Dynamics and Modal Analysis of Slurry Pump Rotor Based on Bidirectional Fluid-Structure Interaction

Guangjie Peng

Research Center of Fluid Machinery Engineering and Technology, Jiangsu University, Zhenjiang, 212013, China.
Key Laboratory of Fluid Machinery and Engineering, Xihua University, Sichuan, 610039, China.

Qi Yin, Lie Ma, Shiming Hong and Guangchao Ji

Research Center of Fluid Machinery Engineering and Technology, Jiangsu University, Zhenjiang, 212013, China.

Hao Chang

Research Center of Fluid Machinery Engineering and Technology, Jiangsu University, Zhenjiang, 212013, China.
Mechanical & Power Engineering College, China Three Gorges University, Yichang, 443000, China.
Fluid Machinery of Wenling Research Institute, Jiangsu University, Wenling, 318000, China.
Leo Group Co., Ltd., Wenling, 317500, China. E-mail: changhao@ujs.edu.cn

(Received 25 April 2024; accepted 28 October 2024)

Slurry pumps are widely used in complex media and harsh operating conditions due to their good transport performance and non-blocking characteristics. This paper takes a slurry pump as the research object, intending to analyze the impeller's structural characteristics and ensure the rotor's safe operation. By combining theoretical analysis and numerical simulation, the dynamic stress characteristics and vibration characteristics of the slurry pump structure are systematically analyzed using the bidirectional fluid-structure interaction research method, and the dry and wet modes of the pump rotor are analyzed. The results show that: the equivalent stress and deformation are the most severe under small flow conditions, and decrease with the increase of flow rate; the maximum equivalent stress occurs at the junction of the trailing edge of the suction surface of the blade and the back cover plate; the maximum deformation occurs at the intersection of the outlet of the impeller flow passage and the back cover plate; the wet mode has a lower inherent frequency than the dry mode; the rotor's inherent frequencies have some equal values of adjacent orders; the rotor's critical speed is 3408.4 r/min, far higher than the rotor's actual speed of 1480 r/min, and will not cause resonance.

1. INTRODUCTION

Slurry pumps are a type of centrifugal pump that is used to transport solid-liquid mixtures. They are widely used in industrial fields such as metallurgy, mining, and hydraulic dredging. Due to the diversity and complexity of the transported medium, the internal flow medium causes severe wear on the slurry pump, and the complex non-steady flow generated by the complex internal flow field and the asymmetry of the volute structure will impose a fluid excitation force on the impeller.[1] In addition, the static load of the rotor itself will also cause the impeller to vibrate and deform, resulting in stress concentration and damage to the structure. The rotor is the core component of the slurry pump and the only actively moving part of the slurry pump when it is working. Therefore, the safe and stable operation of the rotor is an important factor affecting the service life of the slurry pump. The mode is the inherent vibration characteristic of the structure itself. Analyzing the mode characteristics of the rotor to obtain the inherent frequency and mode shape is important for preventing structural damage in advance and optimizing the pump body structure. In addition, when the hydraulic excitation frequency is close to the rotor's inherent frequency, it is easy to produce resonance, which can damage the rotor structure. Therefore, analyzing the mode characteristics of the rotor under environmental conditions is also of guiding significance for the safe operation of the pump.

Early research on fluid-structure interaction theory was mainly concentrated in the aerospace field. In recent years, with the increasing importance of rotating machines in engineering, the FSI problem of turbine machines has also been studied in more depth.[2–6] With the development of numerical simulation technology, the application of FSI technology has become increasingly mature, and gradually formed a systematic study. Peric et al.[7] conducted early research on fluid-structure interaction, realizing the transmission of data such as pressure and displacement on the coupling surface. Pan et al.[8] analyzed the inherent frequency and mode shape of the pump rotor in air and flow field to avoid the occurrence of resonance during the operation of the jet pump and determined the relationship between stress and deformation and speed. Birajdar et al.[9] proposed that there is always interaction between fluid and structure and proposed a unidirectional fluid-structure interaction method to predict the vibration of the pump under special conditions and the influence of blade spacing on vibration displacement. Zhang et al.[10] conducted numerical re-

search on bidirectional fluid-structure interaction for vertical axial pumps. By comparing the analysis of the flow field and the structural field at the corresponding positions, they revealed the relationship between the time and frequency of fluid pressure pulsation and structural vibration at the same position of the vertical axial pump. This provides theoretical guidance for subsequent optimization design and safe operation.

Rotor dynamics research covers multiple aspects, such as inherent frequencies, mode shapes, critical speeds, and dynamic responses, which can be used for modal analysis, vibration analysis, and structural fatigue life prediction.[11–13] Scholars have made great progress in the study of rotor dynamics: Zhou et al.[14–16] used the finite difference method to establish the Reynolds equation for the bearing and solve it, confirming that the influence of the seal on the rotor is not negligible. Jiang et al.[17] conducted a further simulation analysis on the influence of the ring seal and rotor system in a multistage pump on critical rotation and unbalanced response. Through two different solution methods, they found that the stability of the rotor would be affected to different degrees under different lengths and diameter ratios of the seal components. Wang et al.[18] studied the correlation between the dynamic characteristics of the annular rotor and the stability of the bearing system. Based on the results of experiments and theories, they proposed the relationship between the stiffness coefficient of the rotor and the operating frequency, which provides empirical evidence and reference for the optimization of rotor components in the future. Sun et al.19 conducted finite element analysis and rotor dynamics analysis on the slurry pump and obtained the inherent frequency and mode response under different constraints, and determined the critical speed of the rotor, which provides safety guarantees for the operation of the rotor

After the above analysis, it is found that scholars have conducted extensive and in-depth research on the fields of fluid-structure interaction and rotor dynamics of pumps. They have made outstanding contributions to reducing mechanical vibration, reducing rotor failures, and improving pump life. However, the research objects of these aspects are mainly concentrated in ordinary centrifugal pumps. For slurry pumps with higher wear and easier damage, research is still in its infancy. In addition, previous research on pump fluid-structure interaction typically uses unidirectional fluid-structure interaction, which has lower calculation accuracy than bidirectional fluid-structure interaction and cannot perform dynamic stress analysis. This paper will optimize the performance parameters of the slurry pump, combine the bidirectional fluid-structure interaction method to analyze the dynamics of the impeller and the mode of the rotor, obtain the dynamic stress characteristics of the impeller, and analyze the mechanical characteristics of the rotor.

2. SIMULATION EXPERIMENTS AND UNSTEADY CALCULATION

2.1. Model Establishment And Meshing

This paper takes an LC-25 slurry pump as the research object. According to the wooden mold drawings of the model, the impeller and volute of the slurry pump were modeled in three dimensions using UG software, and the water body of the impeller and volute were generated using SpaceClaim software. At the same time, to reduce the influence of inlet and outlet backflow on the convergence of the calculation, the inlet extension section and outlet extension section were extended as 5 times the diameter of the pipe as the inlet extension section and outlet extension section. The specific three-dimensional model of the fluid domain is shown in Fig. 1. Each part was meshed and its boundary layer was refined to strictly ensure that the quality of the fluid domain mesh was above 0.3, and the angles were all greater than $18°$. In addition, the $y+$ of key surfaces such as blades was less than 20, which can fully meet the grid requirements of the SST $k-\omega$ turbulence model near the wall.[20] The mesh model is shown in Fig. 2. Considering the calculation accuracy and cost comprehensively, a mesh model with a mesh number of $3,003,478$ was selected for subsequent numerical analysis. Currently, the number of meshes in the inlet extension section was $647,559$, the number of meshes in the water body of the impeller was $885,210$, the number of meshes in the water body of the volute was $1,073,728$, and the number of meshes in the outlet extension section $is396,981$.

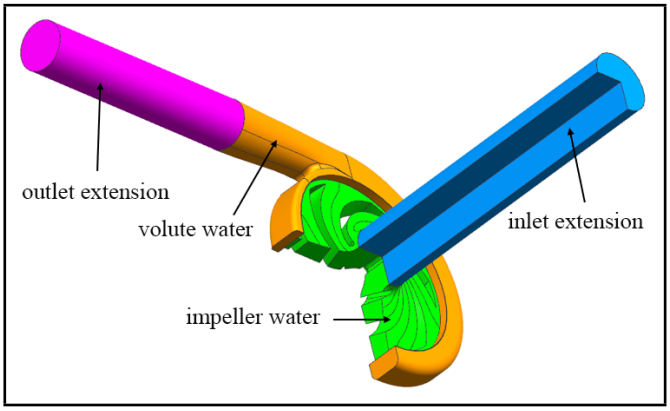

Figure 1. Fluid domain models of slurry pump.

2.2. Boundary Conditions And Parameter Settings

CFX software was used to numerically calculate the slurry pump, using pure water as the medium, and the medium temperature is 298 K. The impeller was set as the rotating domain, and the inlet extension section, volute, and outlet extension section were set as the stationary domain. The turbulence model adopted the shear stress transport model SST $k-\omega$, using a total pressure inlet (1 atm, reference pressure is 0 atm), and mass flow rate outlet (831.66 kg·s-1). The rated speed is 1480 r/min, the interface adopts the frozen rotor method, and the convergence accuracy was 1.0×10^{-5}.

2.3. Experimental Verification

To further verify the accuracy of the numerical simulation results, experimental research on the slurry pump under different operating conditions was carried out. The comparison of experimental and simulated external characteristics is shown in Fig. 3. Slurry pump hydraulic performance tests were conducted on an open test bench at the National Pump and System Engineering Technology Research Center at Jiangsu University. Nine operating points of $0.6Q_d-1.4Q_d$ were selected for the test. The actual image of the slurry pump test bench is

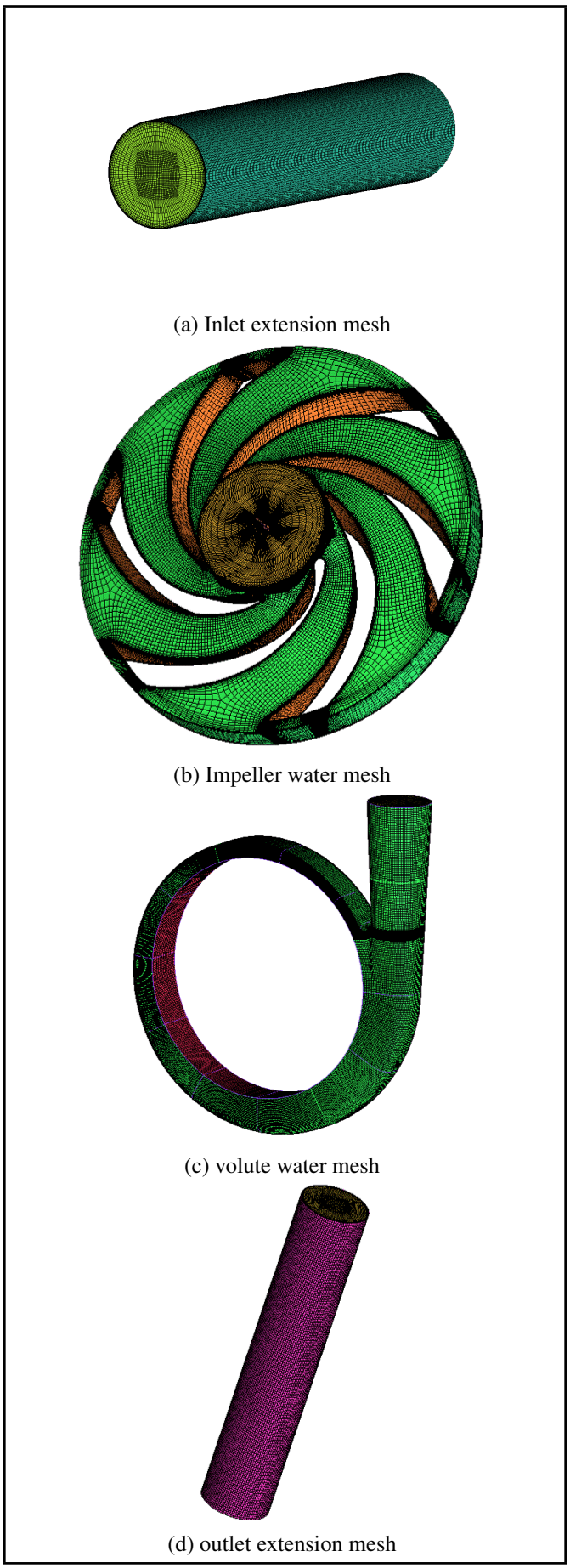

(a) Inlet extension mesh

(b) Impeller water mesh

(c) volute water mesh

(d) outlet extension mesh

Figure 2. Computing domain grid.

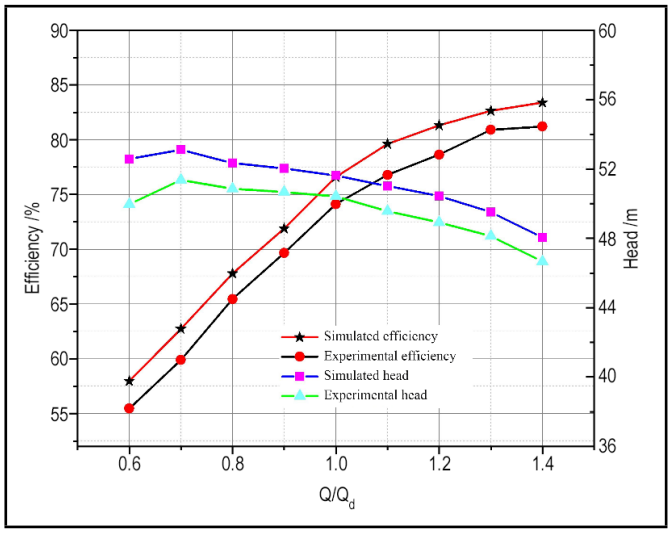

Figure 3. Comparison of external characteristics between test and simulation.

shown in Fig. 4. It can be seen from the figure that the simulation results are in good agreement with the experimental results. The maximum efficiency difference is 2.83 %, the relative error is 3.69 %, the maximum head difference is 2.61 m, the relative error is 5.22 %, and the efficiency difference is 2.48 % at the design condition. The relative error is 3.35 %, the head difference is 1.2 m, the relative error is 2.38 %, which meets the allowable error range of the experiment, ensuring the accuracy of the numerical simulation analysis.

2.4. Unsteady Numerical Computation

In this paper, unsteady numerical calculations were performed for three flow rates of $0.6Q_d$, $1.0Q_d$, and $1.2Q_d$. The results of the steady calculation were used as the initial conditions. The transient settings in CFX were based on the steady settings, with Analysis Type set to Transient and Frame Change/Mixing Model set to Transient Rotor Stator. The results of the calculation were for 10 revolutions of the impeller. The maximum number of iteration steps was set to 5, the duration was set to 0.000337838 seconds, i.e., one time step was set for every 3° rotation of the impeller, the total number of time steps was 1200, the total time was 0.4054 seconds, and the convergence accuracy was set to 10^{-5}. In the calculation process, the following physical quantities were monitored: head, efficiency, mass flow rate at the inlet and outlet of the pump, and radial force. In Trn Result, the flow field was obtained once every 30 steps, i.e., every 90° rotation of the impeller. The settings were the same for all operating points except for the flow rate.

3. FLUID-STRUCTURE INTERACTION NUMERICAL CALCULATION

3.1. Model Establishment And Grid Partitioning

he rotor system of the slurry pump consists of the impeller, pump shaft, and shaft supports, as illustrated in Fig. 5. The impeller and shaft were in direct contact, while the shaft system also incorporates sealing structures and couplings. Both the pump shaft and impeller were fabricated from structural steel

(a) Test bench

(b) Flow transmitter

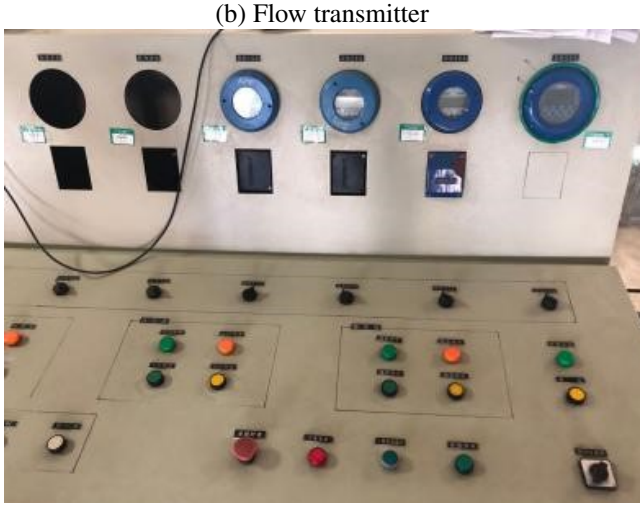

(c) Monitoring station

Figure 4. Testing apparatus.

material. The characteristic parameters of the structural steel are shown in Tab. 1:

The mesh division of the impeller structure was based on adaptive meshing using tetrahedral mesh in the Mesh module, with a total of 178523 elements and 307496 nodes. After inspection, the average quality of the mesh was verified to be above 0.7, meeting the requirements for the mesh division of fluid-structure interaction structures.

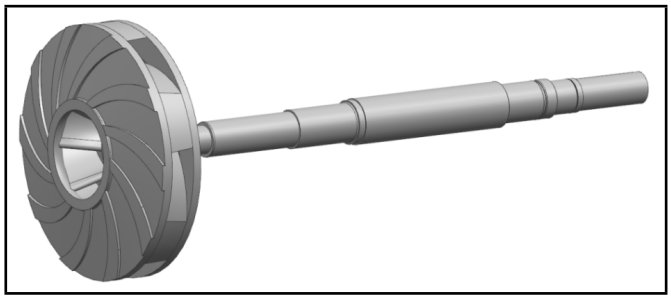

Figure 5. Structure diagram of rotor system.

Table 1. Material attribute table .

Property	Density ρ (kg*m.3)	Elastic modulus E (GPa)	Poisson's ratio μ
Value	7850	200	0.30

3.2. Boundary Condition Settings

The boundary condition settings for the fluid-structure interaction simulation consist of two parts: setting the boundary conditions for the solid domain and setting the boundary conditions for the fluid domain. The coupling calculation was performed using CFX, Transient Structural, and System Coupling modules in Ansys Workbench.

First, the boundary conditions of the solid domain needed to be set, including the material properties of the impeller, as shown in Tab. 1. Next, the constraints were set, including the impeller's own gravity A, the centrifugal force generated by high-speed rotation B (the impeller speed needed to be defined as 1480 r/min at this point), the fixed constraint C, and the fluid-structure interaction interfaces D, E, and F corresponding to the front cover plate, blades, and back cover plate of the impeller, as shown in the yellow part of Fig. 6. Finally, the time step of the structural part is set to be consistent with that of the fluid domain in Analysis Settings. The total simulation time was set to 0.4054 seconds, which corresponds to ten rotations of the impeller, with a time step of 0.000337838 seconds. The Multi-Field Solver was utilized to facilitate information exchange between the fluid and structural domains, enabling iterative solutions of the bidirectional fluid-structure interaction in slurry pump impellers.

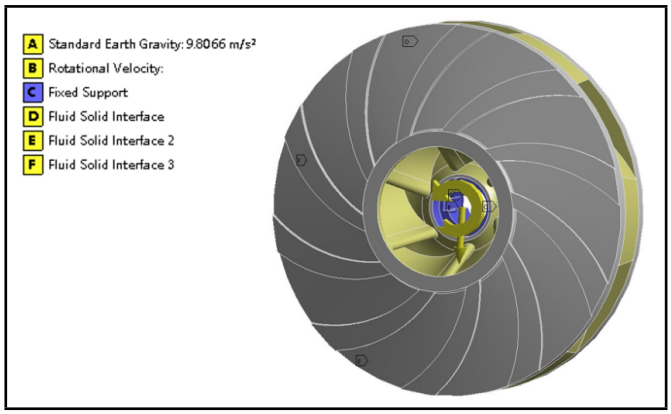

Figure 6. Constraint of impeller.

4. ANALYSIS OF VIBRATION CHARACTERISTICS IN SOLID DOMAINS

4.1. Distribution Of Surface Pressure On Blades

The pressure distribution on the blade surface indicated the stress conditions on the surface when the impeller was working. It was of great engineering significance to clarify the pressure distribution on the blade surface for the stable operation of the impeller. As shown in Fig. 7, the pressure distribution of the impeller blade under different flow conditions ($Q/Q_d = 0.6, 1.0, 1.2$) and different span heights were compared. The horizontal axis represented the relative position along the blade streamline, with a relative position of 0 near the blade root and a relative position of 1 near the blade tip. The vertical axis represented the blade surface pressure value monitored at the relative flow line position, with 0.1 span near the front cover plate, 0.5 span in the middle of the blade, and 0.9 span near the rear cover plate.

It can be seen from Fig. 7 that the blade pressure distribution was composed of two curves, representing the pressure distribution of the pressure and suction surfaces, respectively. The difference between the pressure and suction surfaces was the blade load. Overall, the pressure distribution under various flow conditions has similar laws. With the increase of the relative flow line position, the blade pressure generally shows an upward trend. With the increase of flow, the pressure difference between the pressure and suction surfaces gradually decreases, which means that the blade load gradually decreases. Under the small flow condition, the pressure distribution of the blade fluctuated violently at the blade root. This was because the fluid enters the impeller flow channel and collides with the impeller root, and the flow direction changes under the action of the blade, resulting in pressure turbulence. The pressure on the pressure and suction surfaces maintains a uniform upward trend, but the growth trend of the pressure surface was significantly higher than the growth trend of the suction surface, which made the surface load of the blade gradually increased. When approaching the vicinity of the blade tip, the pressure growth rate of the pressure surface decreased, and after reaching the maximum, it began to decrease. At this time, the suction surface pressure was still increasing. At this point, the blade load decreases. When the blade tip was reached, the pressure distribution on the suction and pressure surfaces is the same, which was called the load zero point, which was affected by the dynamic and static interference between the impeller and the volute tongue.

By comparing the design working condition and the large flow condition, there was also a phenomenon of sudden pressure change near the blade inlet. Then, the working surface pressure first increases and then decreases, and the suction surface pressure continues to increase. The difference is that with the increase of flow, the load zero point gradually moves away from the blade outlet edge.

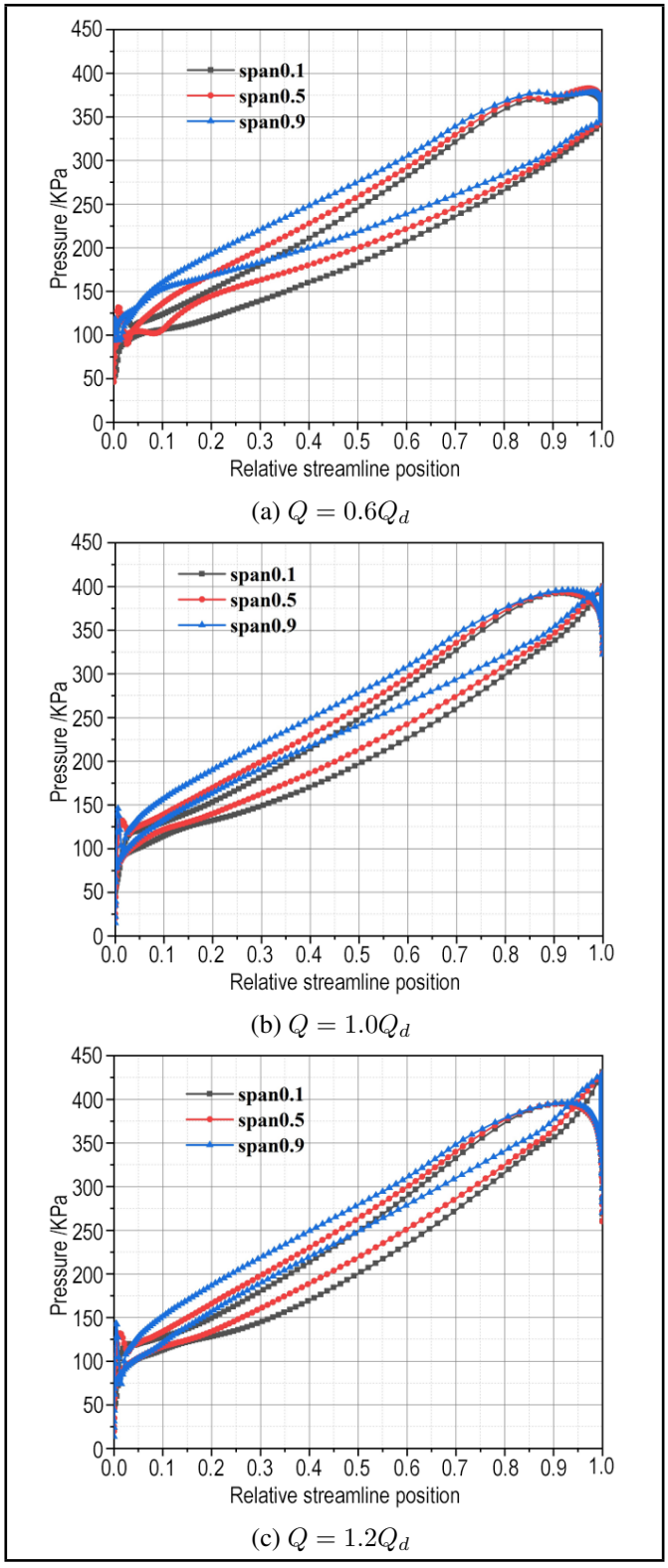

Figure 7. Blade surface pressure distribution under different flow conditions.

5. ANALYSIS OF BLADE DEFORMATION AND STRESS

Table 2 shows the maximum equivalent stress and maximum total deformation under small flow conditions, design conditions, and large flow conditions. The changing trend of maximum equivalent stress and maximum total deformation was consistent, both occurring under small flow conditions. This indicates that the alternating load acting on the small flow con-

Table 2. Maximum equivalent stress and maximum total deformation under different flow conditions.

Operating conditions	$0.6Q_d$	$1.0Q_d$	$1.2Q_d$
Maximum equivalent stress (MPa)	17.284	16.390	15.885
Maximum total deformation (mm)	0.004358	0.003790	0.003545

dition was the strongest. With the increase of flow, the maximum equivalent stress and maximum total deformation decreased slightly.

Figure 8 shows the variation law of the maximum equivalent stress and maximum total deformation of the impeller under different working conditions ($Q/Q_d = 0.6, 1.0, 1.2$) with the rotation of the impeller (taking the results of the numerical calculation of the eighth to tenth circles of the bidirectional fluid-structure interaction). The maximum equivalent stress and maximum total deformation both show a significant decreasing trend with the increase of flow. The difference was that with the increase of flow, the upper and lower fluctuation difference of the maximum equivalent stress was almost the same, while the fluctuation range of the maximum total deformation decreases significantly with the increase of flow. This is because the static pressure in the fluid domain decreases gradually with the increase of flow, and the force acting on the impeller decreases.

Under different flow conditions, there are obvious periodicities. The maximum equivalent stress and maximum total deformation under different flow conditions had 6 large peaks and valleys, which were equal to the number of impeller blades. The fluctuation was particularly obvious under small flow conditions. This shows that the impeller vibrated less under large flow conditions and the flow is more stable. The maximum equivalent stress increases first and then decreases, and then increases again. The maximum total deformation increases first and then decreases, but the maximum equivalent stress reaches the highest point when the maximum total deformation also reaches the maximum value. In the previous context, we learned that the maximum equivalent stress and maximum total deformation trend are the most obvious under small flow conditions ($Q/Q_d = 0.6$). The alternating load acting on it is the largest, and it is very easy to cause structural fatigue damage. Now, we will analyze the change of the maximum equivalent stress and maximum total deformation of the impeller in the last cycle under small flow conditions, and study the change of the dynamic characteristics of the impeller under bidirectional fluid-structure interaction. Figure 9 shows the distribution of equivalent stress in the last cycle of the impeller under small flow conditions ($Q/Q_d = 0.6$), and the unit is MPa. The parts with high equivalent stress were relatively concentrated. The equivalent stress of the front cover plate and the rear cover plate was distributed circumferentially. The parts with high stress were mainly concentrated around the inlet of the impeller. This was because the fluid impacts the impeller inlet area more strongly when the fluid enters the impeller flow channel from the inlet pipe. The stress at the back of the front cover plate was relatively small, which indicated that the existence of the back blade can effectively improve the strength of the front cover plate of the impeller, resulting in a significant reduction in equivalent stress. The equivalent stress of the blade gradually increased from the middle section of the blade to the two ends of the blade. The maximum

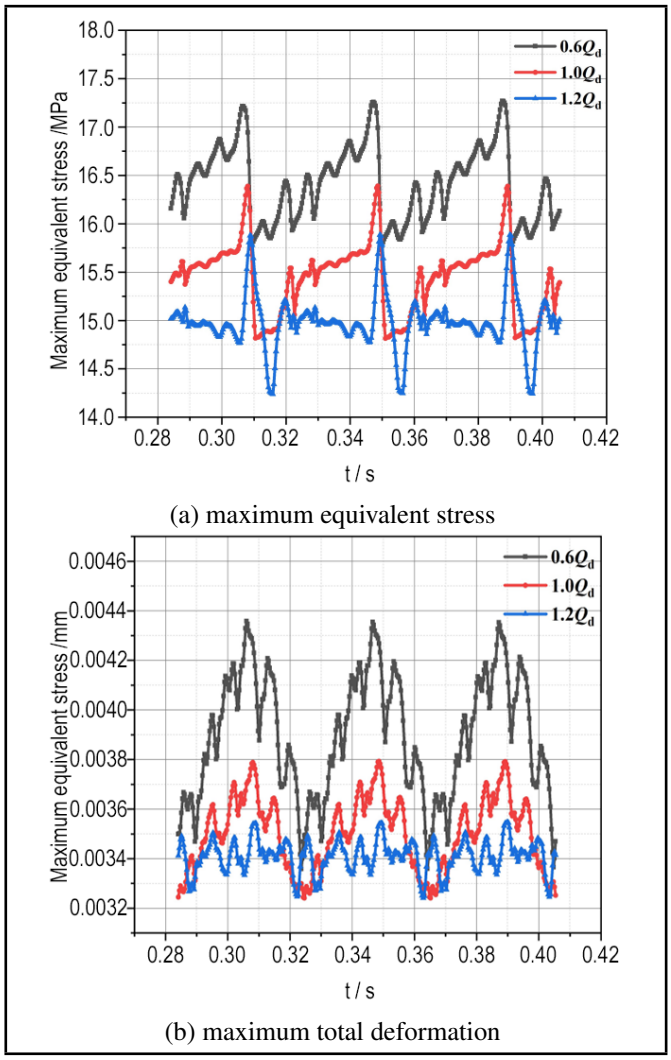

Figure 8. Time domain variation of maximum equivalent stress and deformation under different flow conditions.

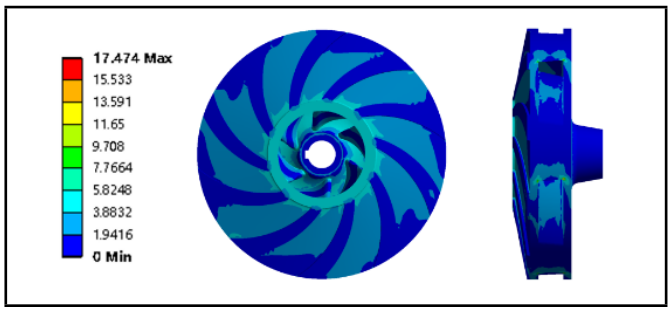

Figure 9. Equivalent stress of impeller distribution ($Q = 0.6Q_d$).

equivalent stress occurred at the junction of the suction surface trailing edge of the blade and the front and rear covers. This was mainly because the structure of this area was sharp and discontinuous, and the intersection relationship at this position is highly constrained. It cannot be relieved by elastic deformation to alleviate stress, resulting in stress concentration in this area. Under the action of alternating load, it was most likely to occur fatigue failure. On the other hand, because it was located at the outlet of the impeller, the fluid was prone to flow separation phenomenon. The pressure difference between the pressure and suction surfaces increases, and the fluid was discharged, resulting in excessive equivalent stress.

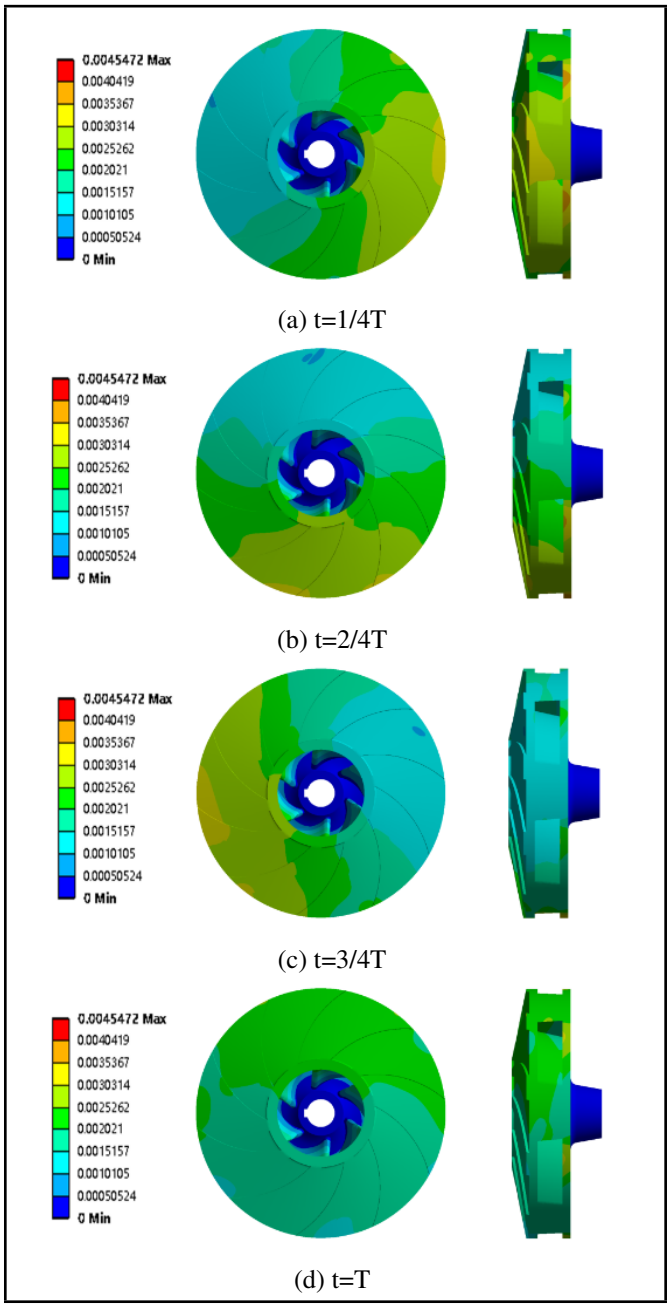

Figure 10. Total deformation of impeller at different time ($Q = 0.6Q_d$).

Figure 10 shows the change of total deformation in the last cycle of the impeller under small flow conditions ($Q/Q_d = 0.6$), and the unit was mm. The total deformation of the front cover plate of the impeller always increases gradually from one side to the other, and presents periodic changes with time. The deformation of the rear cover plate gradually increased from the center to the two ends. The maximum total deformation of the impeller occurs at the intersection of the outlet of the impeller flow channel and the rear cover. Different from the distribution law of equivalent stress, the trend of higher deformation was asymmetric. The total deformation at the same position fluctuates greatly with time, and has a bias. This was because the pressure load was larger at the outlet of the impeller, the centrifugal force was higher, and the radial force generated on the impeller due to the irregular shape of the volute causes the total deformation to fluctuate greatly.

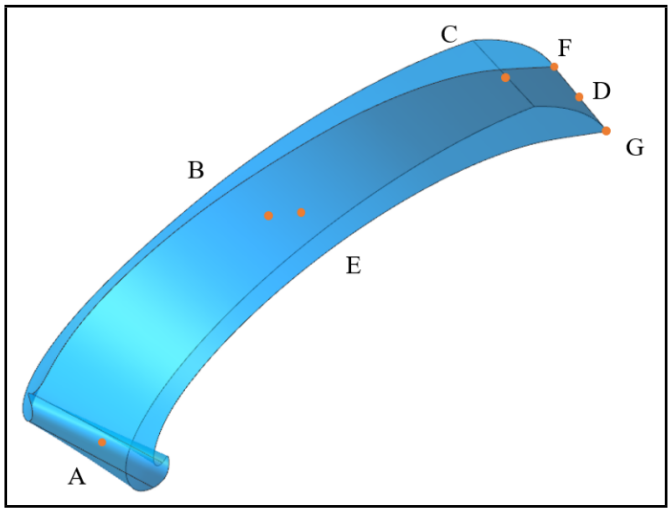

Figure 11. Monitoring points of blade.

5.1. Setting Of Monitoring Points On An Impeller

Figure 11 shows the distribution of different monitoring points on the blade. Point A was located in the middle position of the root of the blade, point B was located in the middle position of the pressure surface of the blade, point C was located in the middle of the pressure surface of the trailing edge of the blade, point D was located in the middle of the trailing edge of the blade near the suction surface, and points F and G were located in the middle of the suction surface of the trailing edge near the front and rear covers, respectively. Point E was in the middle of the suction surface of the blade.

5.2. Dynamic Stress Characteristics of Monitoring Points on the Impeller

Figure 12 shows the variation of the equivalent stress at different monitoring points on the impeller blades under operating conditions $Q/Q_d = 0.6$. Figure 13 shows the frequency domain variation (all calculated from the last five cycles of impeller rotation). The horizontal axis of the frequency domain diagram was f/f_n. As can be seen from the figures, the equivalent stress diagrams at different monitoring points were all periodic, with five large peaks and valleys, which was consistent with the number of impeller rotation cycles. This indicates that the dynamic stress characteristics of the monitoring points were related to the rotation characteristics of the impeller. The frequency domain diagrams show that the main frequency of each monitoring point was still the shaft frequency, and the sub-frequency was in the form of multiples of the shaft frequency. This was the same as the law of fluid domain impeller pressure pulsation, which indicates that the fluctuation of the structural equivalent stress was affected by the fluid pressure pulsation, and reflects the accuracy of the fluid-structure interaction simulation.

Combining Fig. 12 and Fig. 13, the equivalent stress at the monitoring points in the small flow condition was G ¿ F ¿ E ¿ B ¿ A ¿ C ¿ D, and the main frequency amplitude of the pressure pulsation was G ¿ F ¿ A ¿ D ¿ E ¿ B ¿ C. The size of the equivalent stress was not in absolute correspondence with the fluctuation of the pressure. The two monitoring points G, and F located on the suction side of the trailing edge of the blade

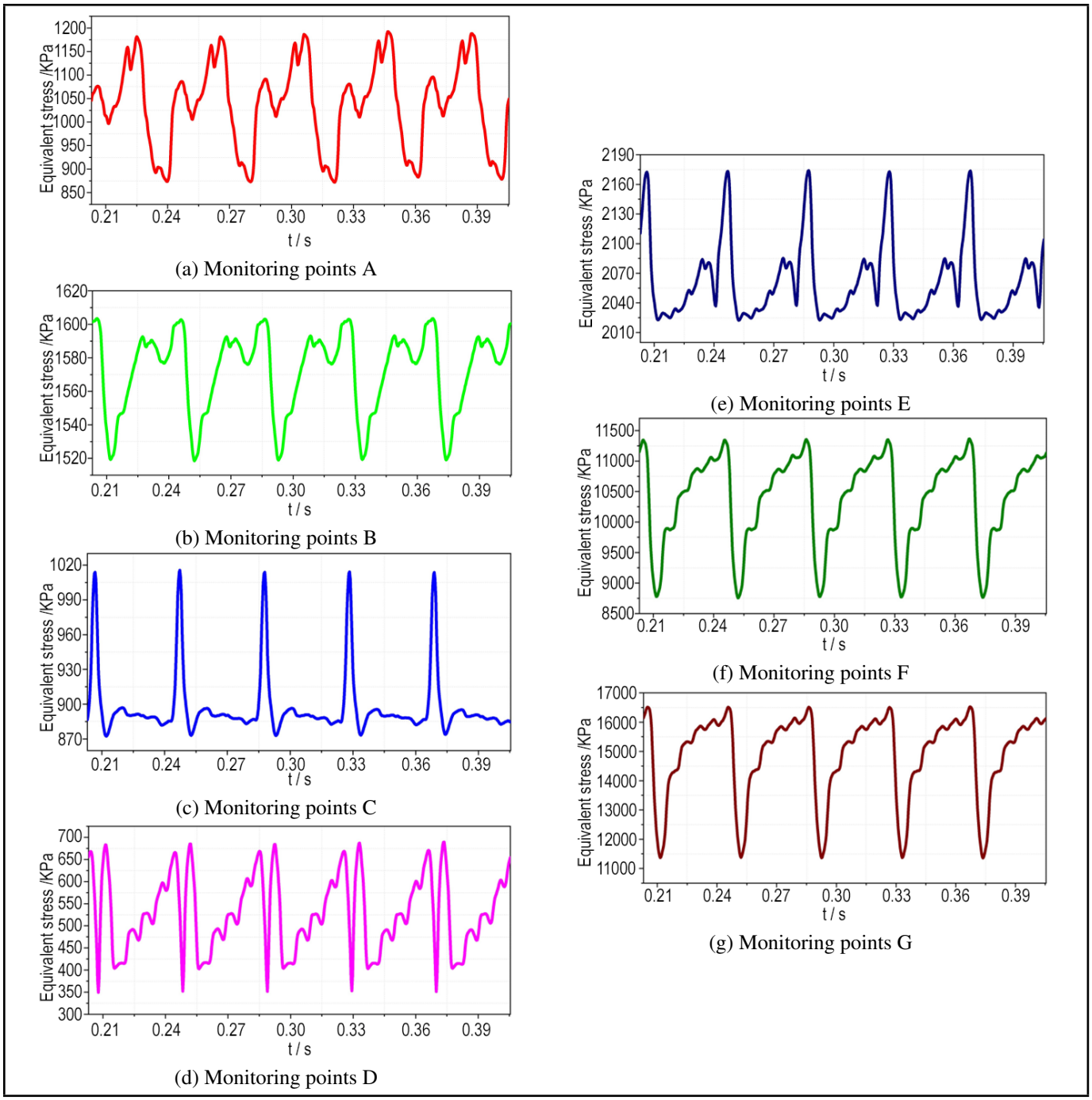

Figure 12. Time domain diagram of equivalent stress($Q = 0.6Q_d$).

have the strongest equivalent stress and pressure pulsation, indicating that this was also the most likely location for fatigue damage. The sharp structure at the tail leads to stress concentration, and the flow separation at the outlet of the fluid is also a cause of the large stress at this location. Therefore, when designing and processing this type of pump, this area should be paid extra attention to. The equivalent stress changes at other monitoring points are much smaller than those at points G and F, but it should be noted that point A at the root of the blade has a smaller equivalent stress but a larger pressure pulsation. This is because the fluid first impacts the root of the blade when it enters the impeller, the fluid velocity changes, and a backflow phenomenon occurs at the root of the blade, resulting in a vortex, causing the vibration at this location to be more violent.

Under the design operating condition and large flow condition, the fluctuation law of the equivalent stress and pressure pulsation at the monitoring points was basically the same as that under the small flow condition. However, with the increase of flow, the equivalent stress and stress fluctuation decrease significantly, indicating that the overall stability of the impeller increases with the increase of flow, further demonstrating that the bidirectional fluid-structure interaction can effectively realize the information transfer between the flow field and the structural field. The difference was that in the large flow condition, there are some nonlinear frequencies near the main frequency at monitoring point A. This was because the increase in flow leads to increased impact losses of the fluid on the root of the blade, causing the fluid to experience small-scale backflow instability at this location. In Fig. 8, it can be observed that the time at which the equivalent stress and total deforma-

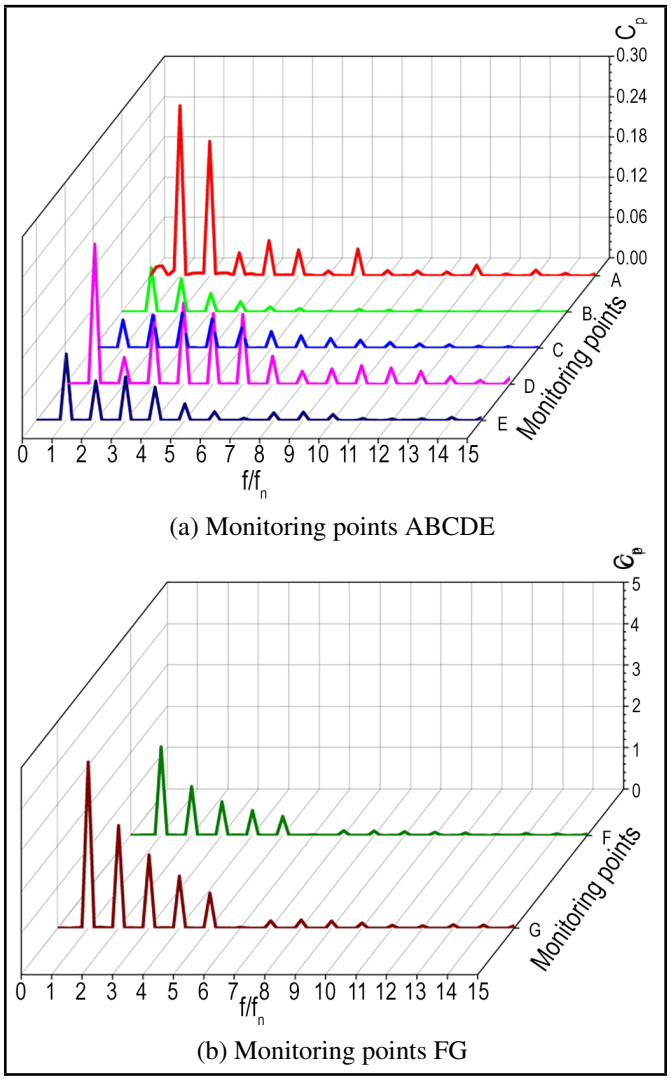

Figure 13. Frequency domain diagram of equivalent stress($Q = 0.6Q_d$).

tion reach their peak values is the same. However, the trends of the equivalent stress and deformation are inconsistent. After being subjected to stress changes, the impeller undergoes deformation, so the deformation at the impeller monitoring points needs to be analyzed. Figures 14 shows the displacement diagrams of each monitoring point as the impeller rotates one revolution under different flow conditions $Q/Q_d = 0.6$. The X, Y, Z axes represent the displacement changes of each monitoring point in the X, Y, and Z directions due to gravity, centrifugal force, and hydraulic excitation force. The red and blue circles represent the positions of the monitoring points before and after deformation, respectively, after one revolution of rotation. Figure 15 shows the difference between the maximum deformation values in the X, Y, and Z directions of each monitoring point under different operating conditions and the undeformed state. Under low flow conditions, all monitoring points undergo displacement deformation in the negative Z-axis direction. The displacement magnitudes in the Z-axis direction follow the order G ¿ D ¿ F ¿ C ¿ B ¿ E ¿ A, with the displacement deformation gradually increasing in the direction of blade outlet. The monitoring points closer to the rear cover plate exhibit higher deformation magnitudes compared to those closer to the front cover plate, which is consistent with the trend of deformation. The deformation magnitudes of the monitoring points at different time instants during impeller rotation vary significantly, with a significant increase from one side to the other. From Fig. 15, it can be observed that under low flow conditions, the order of deformation differences along the X-direction after one revolution of deformation (blue circle) is D ¿ F ¿ E ¿ B ¿ C ¿ A ¿ G, along the Y-direction is F ¿ C ¿ D ¿ A ¿ E ¿ B ¿ G, and along the Z-direction is F ¿ C ¿ D ¿ G ¿ B ¿ E ¿ A. This indicates that the deformation differences in the X, Y, Z directions are inconsistent, suggesting that the impeller undergoes both axial vibration and radial torsional deformation.

Comparing the fluctuation ranges of the monitoring points after one revolution of deformation (blue circle), it can be observed that the curve pattern of the monitoring point A at the root of the blade is the most regular, with almost no up and down vibration. The monitoring points B and E at the middle of the blade exhibit slight up and down vibrations. The monitoring points C, D, F, and G at the trailing edge of the blade show higher vertical fluctuations, with more peaks and valleys. The intense alternating axial vibrations are more pronounced from the root to the trailing edge of the blade, which affects the stability of the trailing edge. Comparing different flow conditions, it is found that under low flow conditions, the fluctuation differences of the blade monitoring points are the highest, indicating more severe vibration and greater susceptibility to damage for the impeller.

In the design conditions, the trend of changes in monitoring points is consistent with that under low flow conditions, but the fluctuation range of deformation is significantly reduced. The increase in flow rate, changes in fluid pressure pulsation, and reduction in radial force are the reasons for this phenomenon. Under high flow conditions, the deformation of each monitoring point has reached a stable state. Although there is still vibration deformation, the difference in deformation is very small. When the impeller rotates one revolution, the difference between each monitoring point and the undeformed state is almost the same, indicating that the impeller is the most stable and has the lowest vibration amplitude under high flow conditions. Using the bidirectional fluid-structure interaction research method to analyze the vibration characteristics of the impeller and obtain deformation data at different positions, has important reference significance for the stability design of slurry pumps.

6. MODAL ANALYSIS OF A PRE-STRESSED SHAFT SYSTEM WITH DRY FRICTION UNDER DRY MODES

In the Ansys Workbench platform, when performing modal analysis with pre-stress on a dry rotor system, the pre-stress cannot be directly applied within the Modal module. Instead, it needs to be set in the Static Structure module first. The results of the Static Structure analysis are then imported into the Modal module to solve for the modes. This section focuses on conducting modal analysis with pre-stress on the rotor components of a dry system. Additionally, a comparative analysis of modes will be performed under different flow conditions, including low flow, design flow, and high flow ($0.6Q_d, 1.0Q_d, 1.2Q_d$).

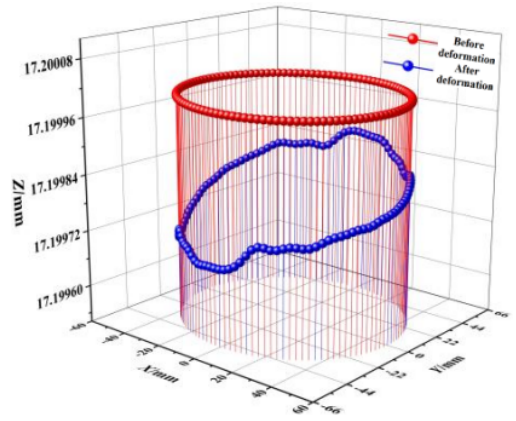

(a) Monitoring points A

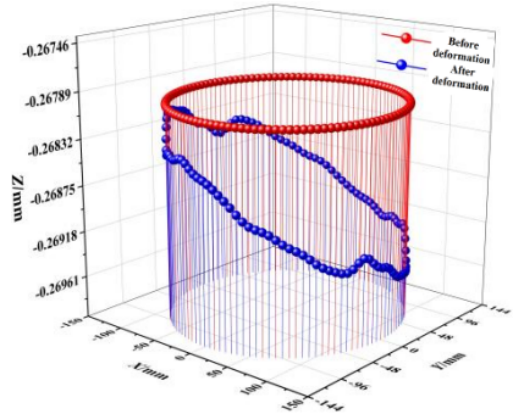

(b) Monitoring points B

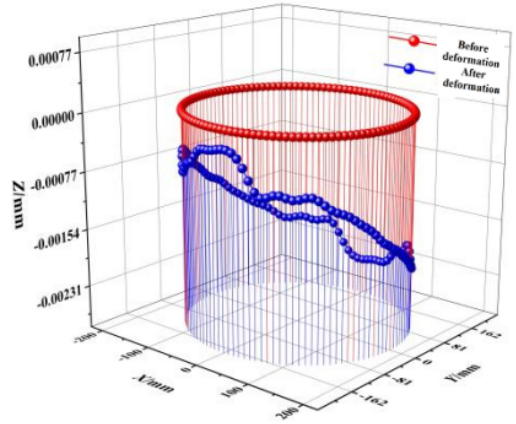

(c) Monitoring points C

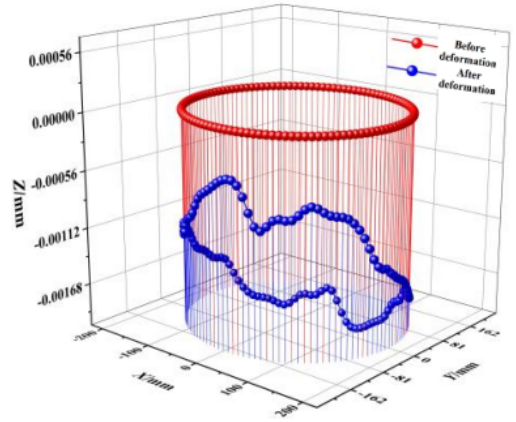

(d) Monitoring points D

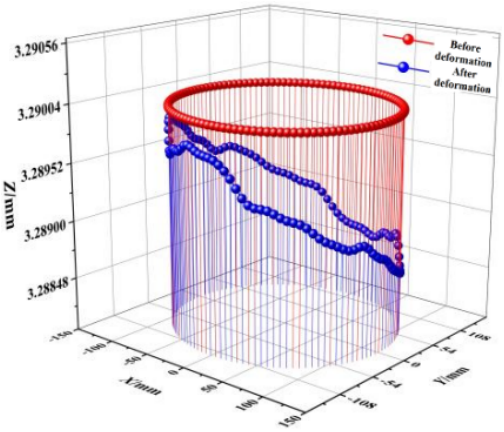

(e) Monitoring points E

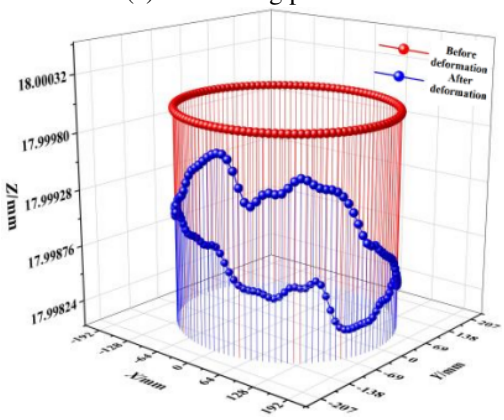

(f) Monitoring points F

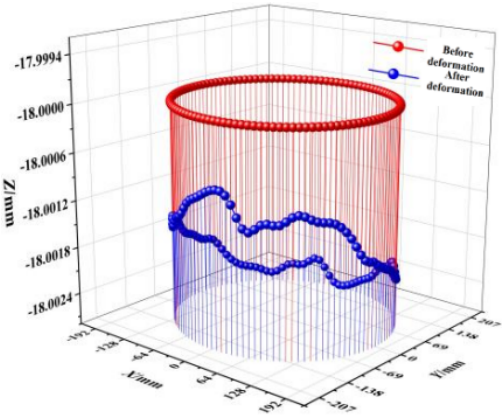

(g) Monitoring points G

Figure 14. Displacement deformation map of monitoring point ($Q = 0.6Q_d$).

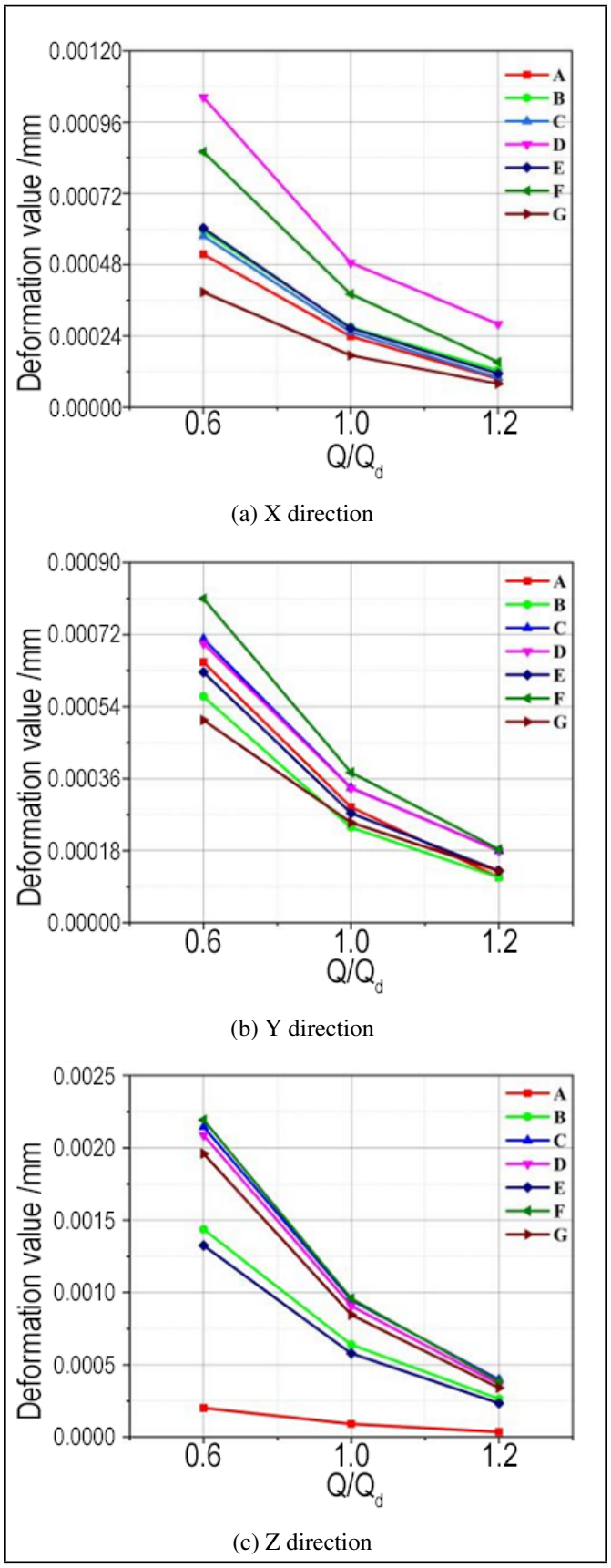

(a) X direction

(b) Y direction

(c) Z direction

Figure 15. Frequency domain diagram of equivalent stress($Q = 0.6Q_d$).

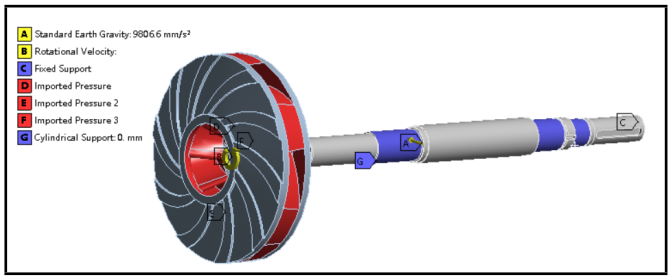

Figure 16. Load vector loading.

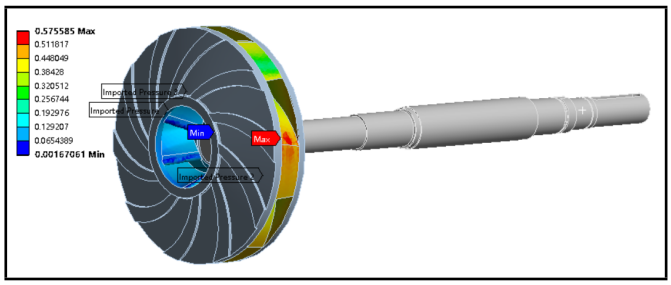

Figure 17. Fluid excitation force distribution.

6.1. Modal Analysis With Pre-Stress In Dry Conditions

Modal analysis with pre-stress in dry conditions refers to the analysis of a shaft system where the rotor is immersed in an air medium. The system is subjected to various forces, including the gravitational force (A) from the rotor components, centrifugal force (B) generated by rotation, cylindrical constraints (G) and fixed supports (C) at both ends of the pump shaft, as well as fluid excitation forces (D, E, F) exerted by the fluid medium on the rotor components. The specific force settings diagram and distribution of fluid excitation forces are illustrated in Fig. 16 and Fig. 17, respectively. From the figure, the minimum value of fluid excitation force was located at the root of the blade and gradually increases outward along the blade. The maximum value was located at the trailing edge of the blade.

After the constraint conditions are set, the rotor components can be analyzed using the Modal module in Ansys Workbench. This allows for the determination of the dry modal results of the slurry pump under pre-stressed conditions. The inherent frequencies increases with the order, as shown in Tab. 3.

6.2. Modal Analysis With Pre-stress Under Different Operating Conditions In Dry Environment

Importing the flow field file at $1.0Q_d$, the first six inherent frequencies of the rotor components of the slurry pump under design operating conditions can be obtained. By using the same solving method, importing the flow field files for the low

Table 3. Dry mode inherent frequencies with prestressing.

Order	Inherent frequencies (f/Hz)
1	49.39
2	49.39
3	74.25
4	296.66
5	296.67
6	797.88

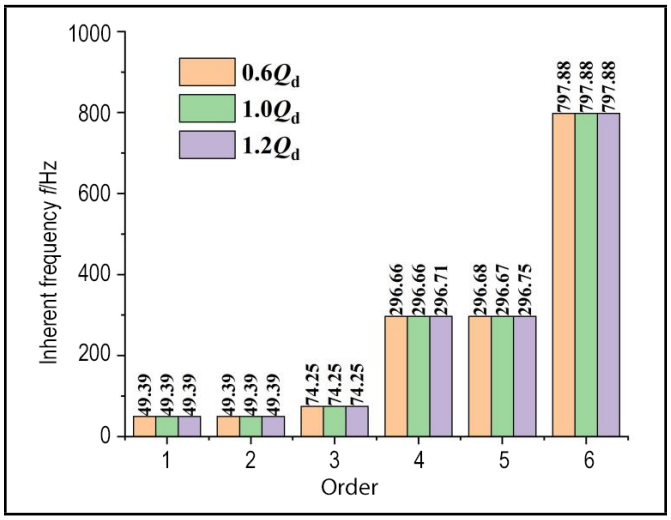

Figure 18. Dry mode inherent frequencies with pre-stressing for different flow conditions.

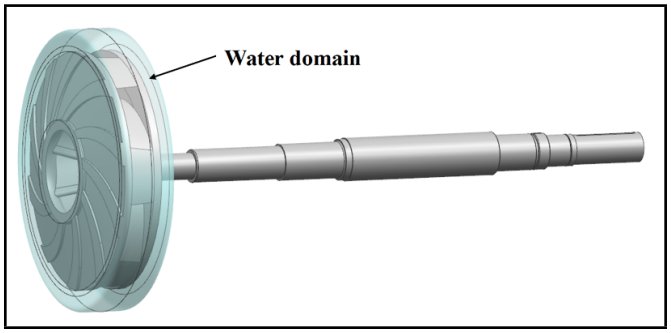

Figure 19. Dry mode inherent frequencies with pre-stressing for different flow conditions.

flow condition ($0.6Q_d$) and high flow condition ($1.2Q_d$) allowed us to calculate the first six inherent frequencies of the pre-stressed rotor components under different operating conditions, as shown in Fig. 18. From the figure, it can be observed that the dry modal frequencies under different operating conditions were essentially the same, with negligible differences. Therefore, when calculating the wet modal analysis of the rotor system subjected to fluid excitation forces, the flow field file from the design operating condition ($1.0Q_d$) will be directly used.

7. MODAL ANALYSIS OF PRE-STRESSED SHAFT SYSTEM UNDER WET CONDITIONS

Modal analysis of pre-stressed rotor components under wet conditions, accounting for the influence of both pre-stress and fluid-induced added mass on the rotor system's modal behavior in an operating medium of water. This analysis provides a closer approximation to the actual working conditions of the rotor system, considering not only the effects of pre-stress on rotor modes but also the impact of fluid-induced added mass on the structural surface during rotor operation in water. The setting conditions for wet modal analysis are more complex compared to dry modal analysis. In addition to the existing dry modal analysis setup, a water domain is added to simulate the rotational modes of rotor components in water, as shown in Fig. 19.

Table 4. Wet mode inherent frequencies with prestressing.

Order	Inherent frequencies (f/Hz)
1	42.03
2	42.06
3	63.31
4	257.83
5	257.86
6	710.85

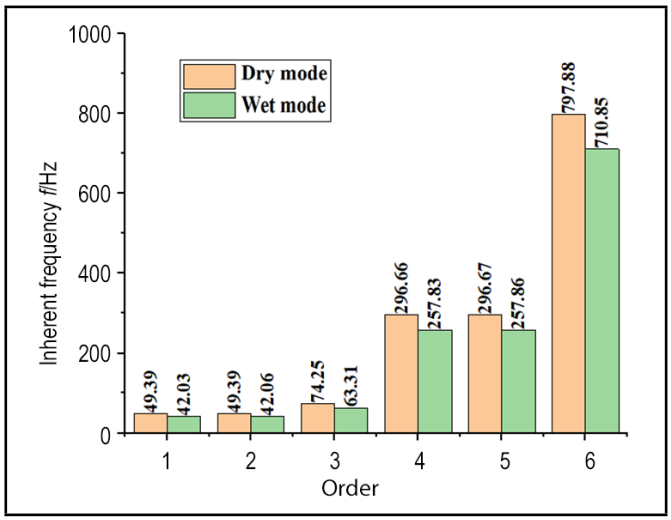

Figure 20. Inherent frequencies comparison between dry and wet condition.

In this study, an acoustics plugin, specifically the acoustics module in Ansys, was employed for the calculation of wet modal analysis. The acoustics module allows for the definition of fluid-structure interaction interfaces, acoustic bodies, and material properties specific to the water domain. These properties include fluid density, elastic modulus, Poisson's ratio, and speed of sound propagation in the fluid. Wet modal analysis of the rotor components was then performed to obtain more realistic inherent frequencies, mode shapes, and critical speeds.

7.1. Inherent Frequencies

The results of the wet mode inherent frequencies of the slurry pump rotor system with preload are shown in Tab. 4, and the comparison of dry and wet mode inherent frequencies is shown in Fig. 20. It can be seen from the figure that the inherent frequencies of the wet mode of the slurry pump rotor system are lower than the dry mode, with a decrease of 10 % to 15 %. This is because the presence of water will produce additional mass on the surface of the structure, thereby increasing the damping of the rotor rotation, and affecting the dynamic characteristics of the structure when it rotates, resulting in the inherent frequencies of the rotor system in water. It can be seen from the relevant literature that the reduction range in each mode is within a reasonable range.[22] It can be inferred from this that based on the difference in medium density, the additional mass on the surface of the rotor structure will also be different, which will in turn affect the results of the mode to varying degrees.

7.2. Mode Shape Diagram

Figure 21 shows the vibration mode diagram of the first 6 orders of wet mode of the rotor components. It can be seen from the inherent frequency Tab. 4 that the inherent frequencies of the adjacent orders of the rotor system are almost the same, such as the first and second, fourth and fifth. This is because the rotor structure is arranged in a periodic symmetrical manner, so the frequency and vibration mode tend to be the same, but the vibration direction is significantly different.

The first-order vibration mode is the bending vibration of the impeller and the top of the pump shaft along the positive direction of X, with a maximum displacement of 6.94 mm, appearing on the outermost front cover plate of the impeller along the negative direction of X. The second-order vibration mode is the bending vibration of the impeller and the top of the pump shaft along the positive direction of Y, with a maximum displacement almost the same as the first order. The third-order vibration mode is the torsional vibration of the rotor around the rotating axis Z. The fourth and fifth-order vibration modes are the combined vibration of the pump shaft swinging in the axial plane and the bending deformation of the impeller. The deformation displacement of the shaft and the impeller are both large, with a maximum displacement of about 9.46 mm. The maximum displacement is also located at the outermost rear cover plate of the impeller. The sixth-order vibration mode is the extension motion of the pump shaft along the Z axis of the rotating axis.

7.3. Critical Speed

Critical speed refers to the speed of the rotor at which resonance occurs during operation. When the rotor is working, the centrifugal force generated by the offset center of gravity causes the rotor to vibrate laterally. When the speed reaches a specific value, the vibration phenomenon will become particularly severe, affecting the operation of the structure, this phenomenon is called resonance. Therefore, the purpose of conducting critical speed research is to keep the actual speed of the rotor system away from the critical speed during operation, thereby avoiding dangerous situations. To ensure the normal operation of the machine, it is stipulated that the critical speed should deviate from the working speed by more than 20 %. In addition, the material structure of the rotor and the boundary conditions set will affect the size of the critical speed, and the rotor system has many orders of mode frequencies in actual operation, and each order of mode corresponds to a critical speed.

The Campbell diagram is a two-dimensional graph based on modal analysis. The horizontal axis represents the speed, and the vertical axis represents the inherent frequency. The diagram contains multiple inclined curves, each inherent mode frequency corresponds to two inclined curves, namely the positive forward motion curve with positive slope change and the negative forward motion curve with negative slope change. The diagram also contains a driving curve. The driving curve starts from the origin of the coordinates, and the frequency of the speed is equal to the inherent frequency. The intersection of the driving curve and the straight line of each inherent mode frequency is the condition of the critical speed of the rotor.

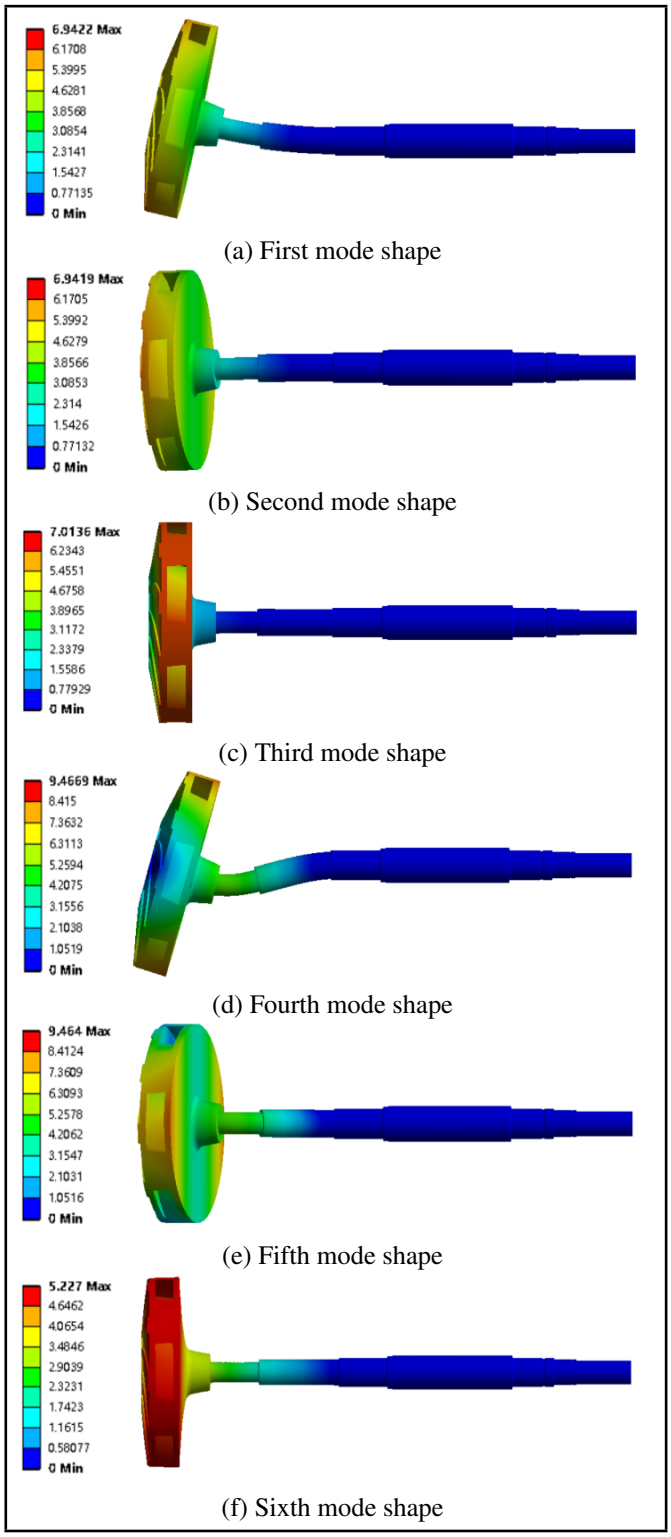

Figure 21. Vibration diagram.

The advance mentioned above refers to the vortex, which is the self-excited vibration caused by the structure itself and the operating conditions, rather than the forced motion caused by external forces. When a rotating structure vibrates, the particles on the rotating axis will move on a fixed trajectory. Then, when the direction around the rotating axis is the same as or opposite to the rotating speed, it is called forward vortex (FW) or backward vortex (BW).

The Campbell diagram for the rotor structure of this model after modal analysis is shown in Fig. 22. Only the first three

Table 5. The rotational speed at the intersection of the excitation line and inherent frequencies curves.

Inherent frequency order	First order	Second order	Third order
Intersection speed (r/min)	2486.3	3408.4	4076.9

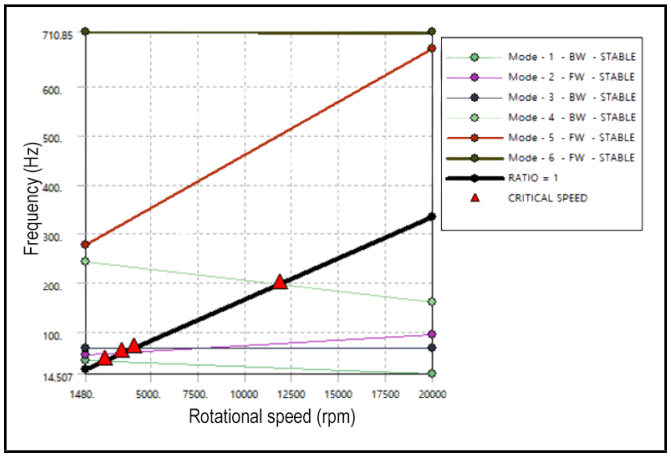

Figure 22. Campbell diagram.

critical speeds were considered in the text, as high-order modal frequencies are usually much higher than the rotor operating frequency and have little significance for studying critical speeds. Because the rotor was subject to unbalanced excitation forces during operation, which caused the rotor to undergo synchronous forward vortex motion, only the vibration frequency of the forward vortex was considered in the process of solving for the critical speed. As can be seen from Table 5, the second order is the frequency of the forward vortex, while the first and third orders are the frequencies of the reverse vortex. Therefore, the critical speed of the pump is 3408.4 r/min, which is much higher than the actual rotor speed of 1480 r/min. The rotor will not resonate under normal operating conditions.

8. CONCLUSIONS

In this study, a systematic analysis of the dynamic stress characteristics and vibration characteristics of the slurry pump structure, as well as the dry mode and wet mode of the pump rotor, was conducted by combining theoretical analysis with numerical simulation, using the bidirectional fluid-structure interaction research method. The following key conclusions were obtained:

1. In the pressure distribution on the blade surface, significant fluctuations are observed at the blade root due to fluid interaction and directional changes. As the relative flow streamlines increase, the overall blade pressure shows an upward trend. However, the pressure on the pressure side increases at a higher rate compared to the suction side. Near the blade trailing edge, the pressure distribution on both the suction and pressure sides aligns (i.e., load zero point). As the flow rate increases, the load zero point gradually moves away from the blade exit edge.

2. At low flow conditions, the stress and strain on the impeller are most severe. The maximum equivalent stress occurs at the junction between the suction side trailing edge and the rear cover plate. This location has a sharp structure and a constrained intersection, leading to stress concentration. It is also situated at the impeller exit, where the flow field is complex and most prone to fatigue damage. The maximum deformation is observed at the intersection of the impeller flow passage exit and the rear cover plate. This is due to the high-pressure load and centrifugal forces at the exit, coupled with significant radial force fluctuations.

3. The trajectories of equivalent stress and displacement at various monitoring points decrease as the flow rate increases. Monitoring points located on both sides of the blade trailing edge experience the highest equivalent stress and pressure fluctuations. Monitoring points at the blade root exhibit higher pressure fluctuation amplitudes, indicating highly unstable flow in this region. Displacement deformation occurs in the negative Z-axis direction at all monitoring points, with deformation increasing along the blade exit direction. The impeller deformation includes both axial vibrations and radial twisting distortions.

4. Inherent frequencies in the wet mode exhibit a trend consistent with the dry mode, with inherent frequencies increasing with the order of the mode. However, inherent frequencies in the wet mode are approximately $10-15\,\%$ lower than those in the dry mode. This reduction is due to the added mass effect of water on the rotor surface, which increases the damping of the rotor and lowers inherent frequencies. Due to the periodic structure of the rotor, some adjacent mode frequencies may be equal, though their vibration directions differ. Additionally, the Campbell diagram indicates that the critical rotational speed is the intersection of the excitation frequency and the natural frequencies of various modes, considering only the positive whirl. The pump's critical rotational speed is 3408.4 rpm, which is significantly higher than the actual rotor speed of 1480 rpm, indicating that resonance is unlikely to occur.

ACKNOWLEDGEMENTS

The authors gratefully acknowledge the support from the National Natural Science Foundation of China (Grant No.52409114), China Postdoctoral Science Foundation (Grant No.2024M751272), Open Research Fund Program of State key Laboratory of Hydroscience and Engineering (Grant No. sklhse-2024-E-02), Open Research Subject of Key Laboratory of Fluid Machinery and Engineering (Xihua University) [grant number LTDL2022006], Open Research Subject of Hubei Key Laboratory of Hydroelectric Machinery Design & Maintenance (China Three Gorges University) [grant number 2020KJX07] and Taizhou Science and Technology Support Plan (Grant No. TG202336).

REFERENCES

[1] Peng G., Lou Y., Yu D., Hong S., Ji G., Ma L., Chang H., Investigation of energy loss mechanism and vortical structures characteristics of marine sediment pump based on the response surface optimiza-

tion method, *J. Mar. Sci. Eng.*, **11**(12), 2233, (2023). https://doi.org/10.3390/jmse11122233

[2] Zhang L., Guo Y., Zhang H., Fully coupled flow-induced vibration of structures under small deformation with GMRES method, *Appl. Math. Mech.*, **31**(1), 87-96, (2010). https://doi.org/10.1007/s10483-010-0109-z

[3] Wang S., Zhang G., Zhang Z., Hui D., Zong Z., An immersed smoothed point interpolation method (IS-PIM) for fluid-structure interaction problems, *Int. J. Numer. Methods Fluids*, **85**(4), 213-234, (2017). https://doi.org/10.1002/fld.4379

[4] Yang J., Preidikman S., Balaras E., A strongly coupled, embedded-boundary method for fluid–structure interactions of elastically mounted rigid bodies, *J. Fluids Struct.*, **24**(2), 167-182, (2008). https://doi.org/10.1016/j.jfluidstructs.2007.08.002

[5] Wang X., Zhang L., Modified immersed finite element method for fully-coupled fluid–structure interactions, *Comput. Mech. Eng*, **267**, 150-169, (2013). https://doi.org/10.1016/j.cma.2013.07.019

[6] Cornejo A., Franci A., Zárate F., Oñate E., A fully Lagrangian formulation for fluid-structure interaction problems with free-surface flows and fracturing solids, *Comput. Struct.*, **250**, 106532,(2021). https://doi.org/10.1016/j.compstruc.2021.106532

[7] Dettmer W., Perić D., A computational framework for fluid–structure interaction: Finite element formulation and applications, *Comput. Methods Appl. Mech. Eng.*, **195**(41), 5754-5779, (2006). https://doi.org/10.1016/j.cma.2005.10.019

[8] Pan X., Pan Z., Huang D., Shen Z., Fluid structure interaction dynamic analysis of a mixed-flow waterjet pump, *IOP Conference Series: Materials Science and Engineering*, **52**(7), 072013, (2013). https://doi.org/10.1088/1757-899X/52/7/072013

[9] Birajdar R., Keste A., Prediction of flow-induced vibrations due to impeller hydraulic unbalance in vertical turbine pumps using one way fluid-structure interaction, *J. Vib. Eng. Technol.*, **8**(3), 417–430, (2020). https://doi.org/10.1007/s42417-019-00174-5

[10] Zhang L., Wang S., Yin G., Guan C., Fluid–structure interaction analysis of fluid pressure pulsation and structural vibration features in a vertical axial pump, *Adv. Mech. Eng.*, **11**(3), 1687814019828585, (2019). https://doi.org/10.1177/1687814019828585

[11] Meng G., A review and prospect of rotor dynamics research, *J. Vib. Eng.*, **01**, 5-13, (2002). https://doi.org/10.6052/1672-6553-2018-075

[12] Luo Z., Wang J., Han Q., Wang D Review on dynamics of the combined support-rotor system, *J. Mech. Eng.*, **57**(7), 44-60, (2021). https://doi.org/10.3901/JME.2021.07.044

[13] Han Q., Ma H., Progress in rotor dynamics research, *J. Dyn. Control*, **16**(06), 481-482, (2018). https://doi.org/10.6052/1672-6553-2018-075

[14] Zhou W., Qiu N., Wang L., Gao B., Liu D., Dynamic analysis of a planar multi-stage centrifugal pump rotor system based on a novel coupled model, *J. Sound Vib.*, **434**, 37-260, (2018). https://doi.org/10.1016/j.jsv.2018.07.041

[15] Zhou W., Wang X., Qiu N., Wang L., Gao B., Effect of annular seal on the lateral-axial bi-direction coupled dynamic characteristics of a multi-stage pump wet rotor [J], *Chin. J. Eng.*, **40**(12), 1540-1548, (2018) https://doi.org/10.13374/j.issn2095-9389.2018.12.013

[16] Wang L., Zhou W., Wei X., Zhai L., Wu G., A coupling vibration model of multi-stage pump rotor system based on FEM, *Mechanics*, **22**(1), 11420, (2016). mechanika.ktu.lt/index.php/Mech/article/view/11420

[17] Jiang Q., Zhai L., Wang L., Wu D., Fluid-structure interaction analysis of annular seals and rotor systems in multistage pumps, *J. Mech. Sci. Technol.*, **27**(7), 1893-1902, (2013). https://doi.org/10.1007/s12206-013-0507-y

[18] Wang C,, Chen H,, Sun W,, Wang H,, Dynamic characteristics of the annular rotor components in a rotor-bearing system under high frequency stress conditions, *J. Phys. Conf. Ser.*, **1183**(1), 012013, (2019). https://doi.org/10.1088/1742-6596/1183/1/012013

[19] Sun J., Xiao J., Dynamic characteristics analysis of the mud transfer pump rotor, *Proceedings of 2013 3rd International Conference on Mechanical Materials and Manufacturing Engineering(ICMMME 2013 III)*, **5**, (2013). kns.cnki.net/KCMS/detail/detail.aspx?dbcode=IPFD&filename=ZNXX201310006049

[20] Hong S., Peng G., Yu D., Chang H., Wang X., Investigation on the erosion characteristics of liquid–solid two-phase flow in tee pipes based on CFD-DEM, *J. Mar. Sci. Eng.*, **11**(12), 2231, (2023). https://doi.org/10.3390/jmse11122231

[21] Chang H., Ji G., Yu D., Peng G.., Hong S., Du J., Research on wear characteristics of U-shaped elbows based on CFD-DEM coupling. *Front. Energy Res.*, **11**, (2023). https://doi.org/10.3389/fenrg.2023.1282739

[22] Wang Q., A comparison of factors influencing the natural frequency of multistage centrifugal pump rotors. *J. Irrig. Drain. Mach. Eng.* **33**(01), 31-36, (2015). https://doi.org/10.3969/j.issn.1674-8530.14.0095

A. FIGURES FOR DESIGN FLOW CONDITIONS AND LARGE FLOW CONDITIONS IN CHAPTER 3

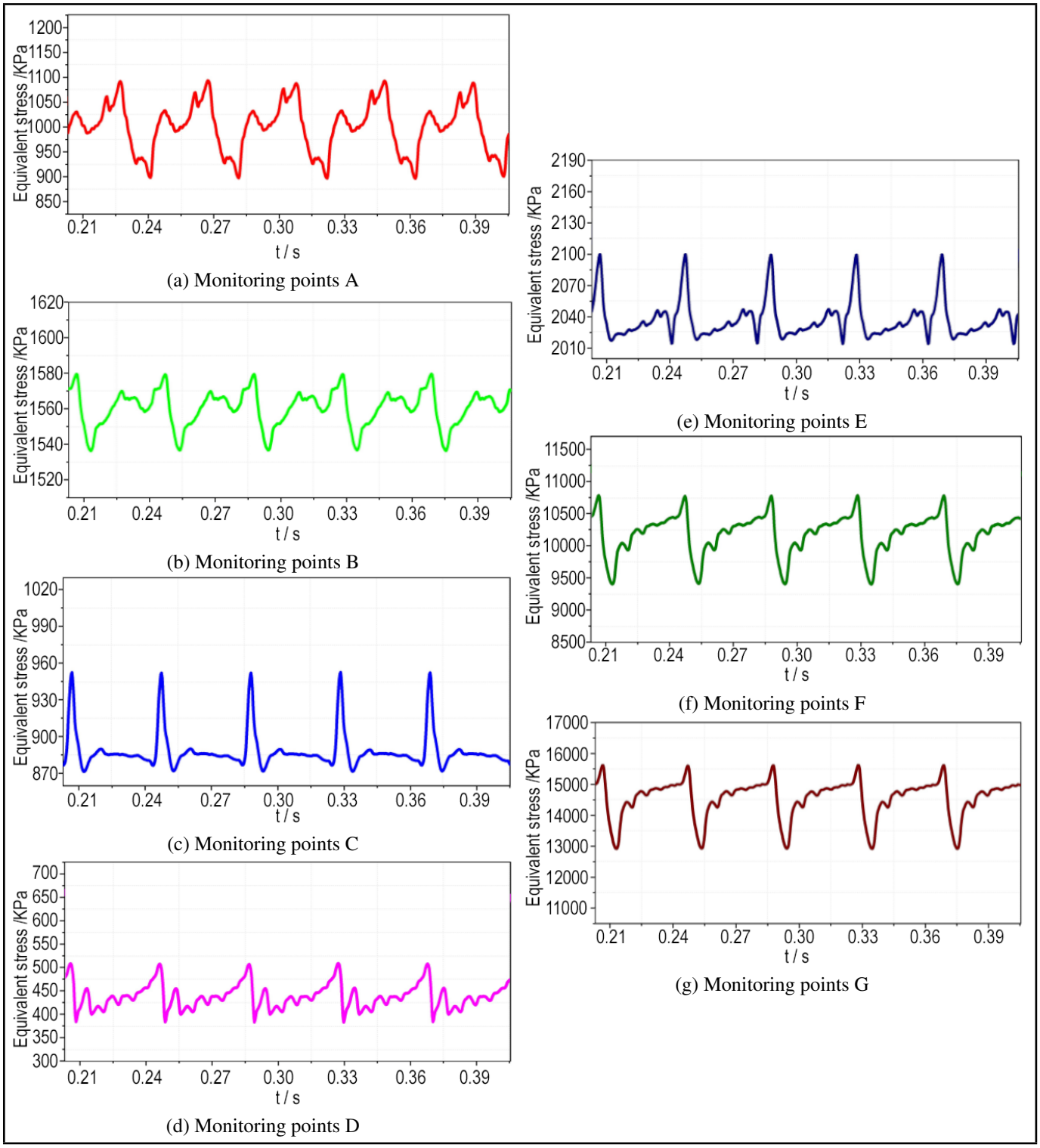

Figure 23. Time domain diagram of equivalent stress($Q = 1.0Q_d$).

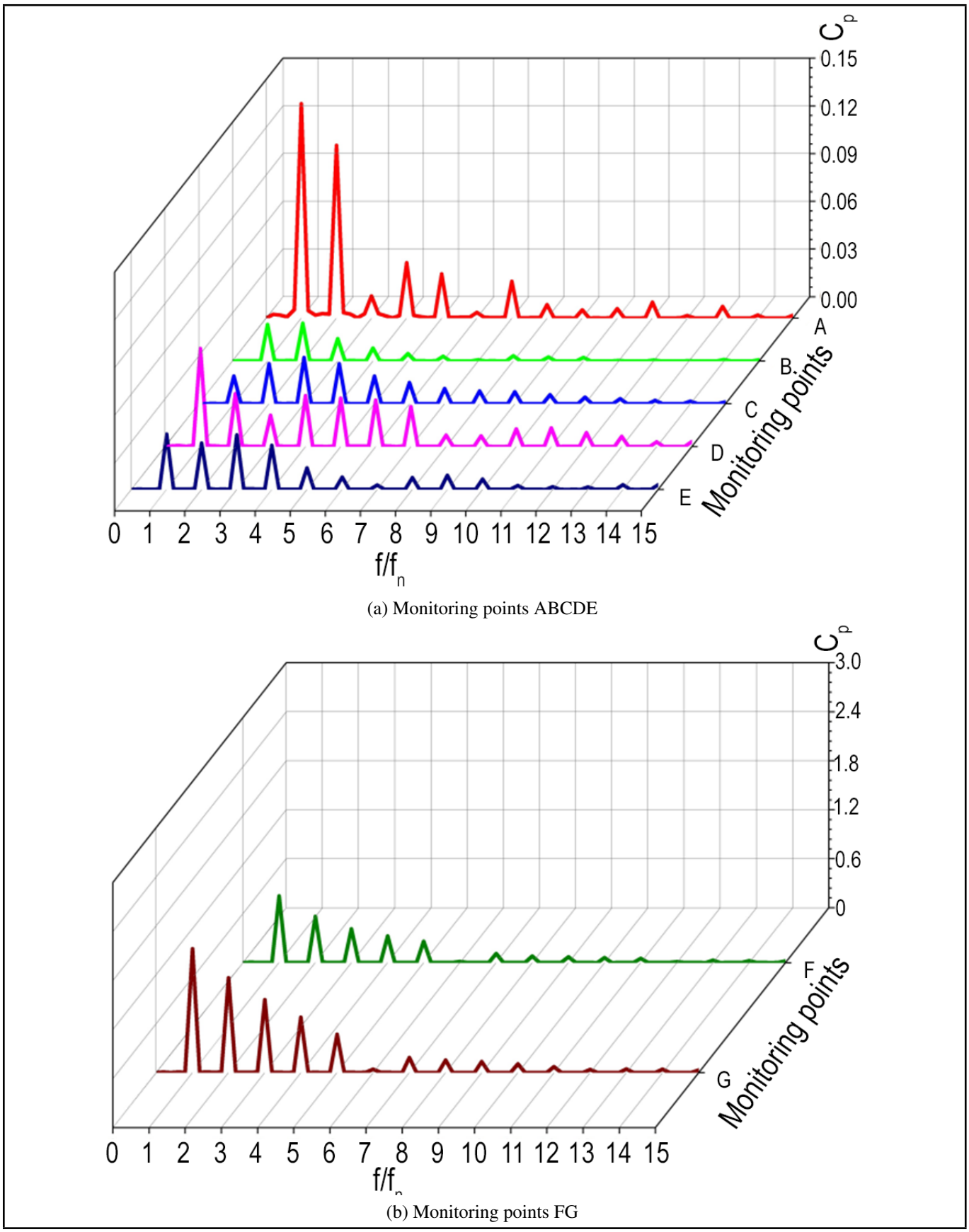

(a) Monitoring points ABCDE

(b) Monitoring points FG

Figure 24. Frequency domain diagram of equivalent stress($Q = 1.0Q_d$).

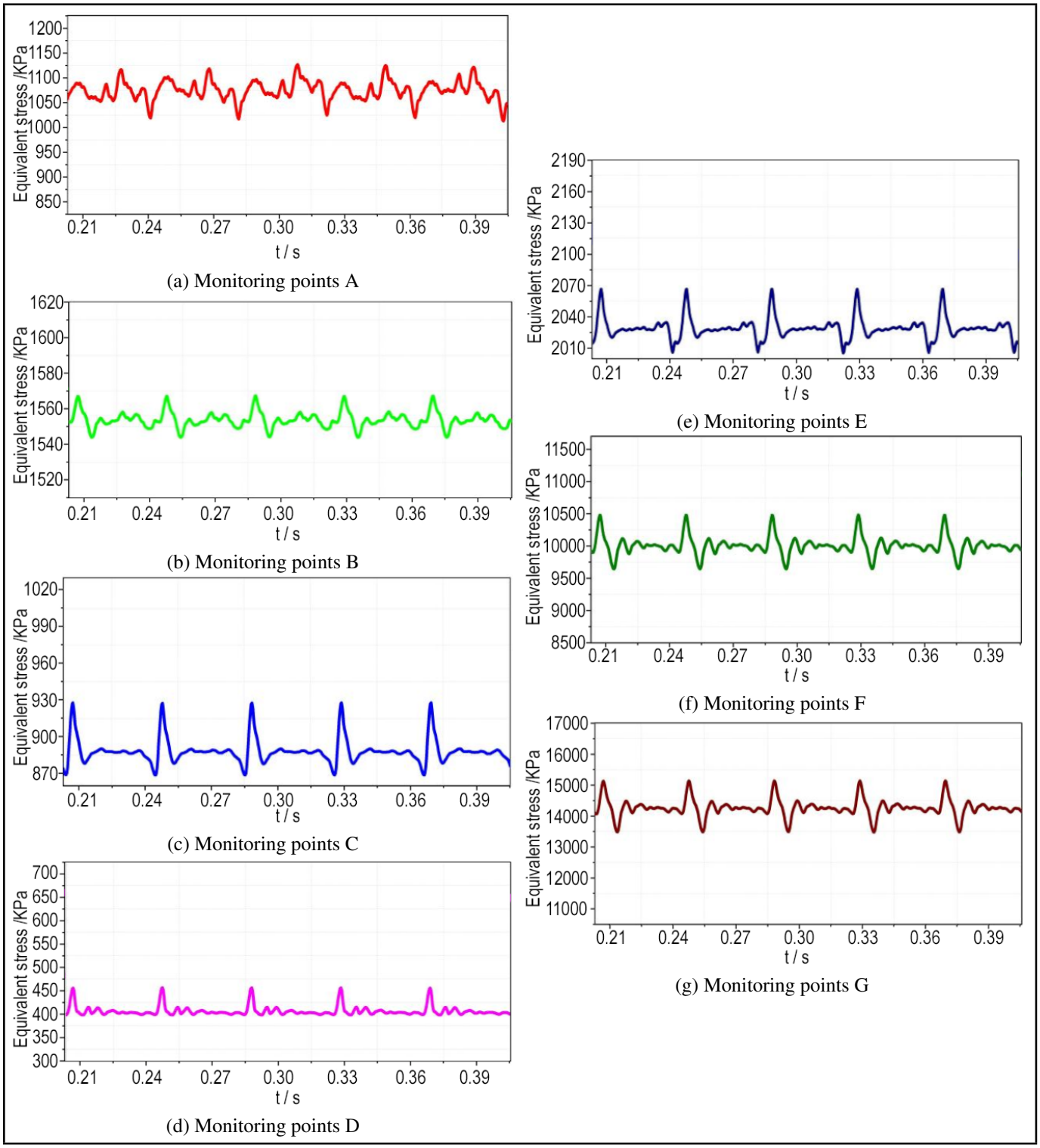

Figure 25. Time domain diagram of equivalent stress($Q = 1.2Q_d$).

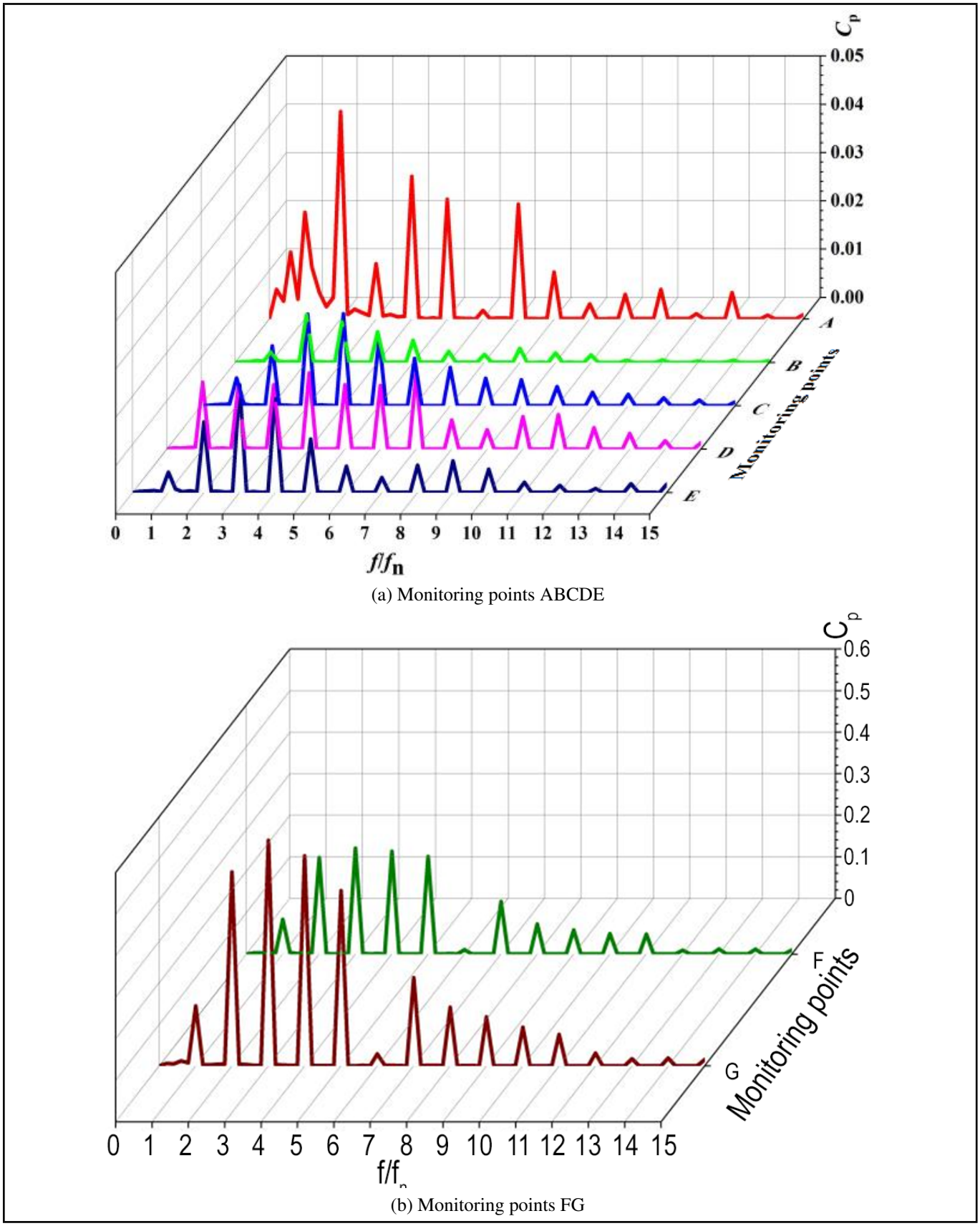

Figure 26. Frequency domain diagram of equivalent stress($Q = 1.2Q_d$).

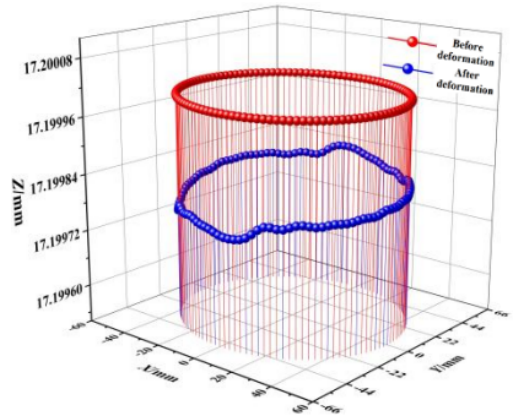

(a) Monitoring points A

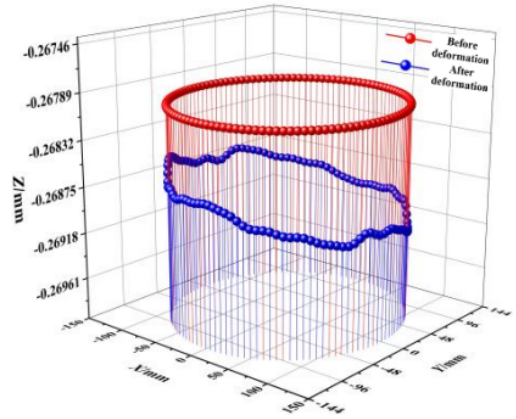

(b) Monitoring points B

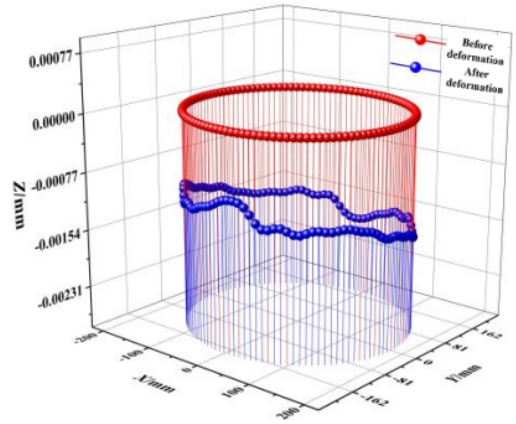

(c) Monitoring points C

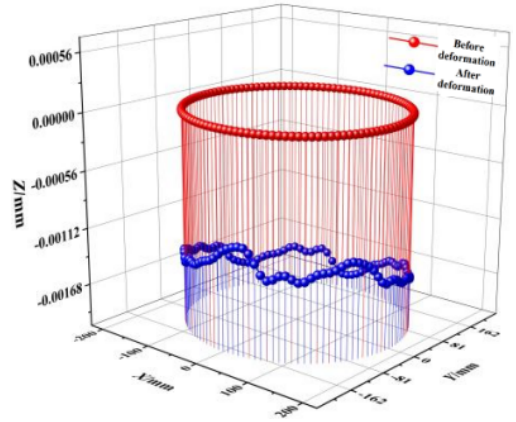

(d) Monitoring points D

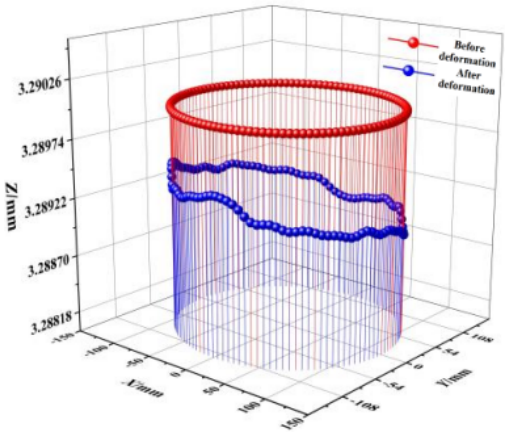

(e) Monitoring points E

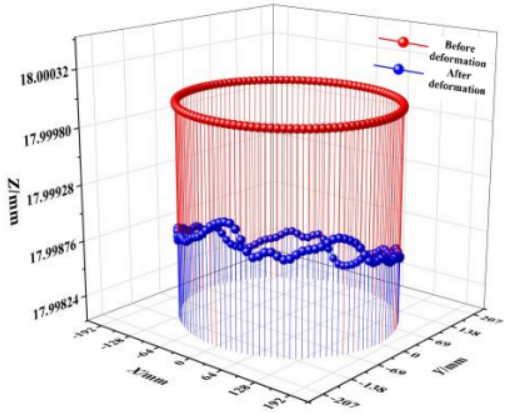

(f) Monitoring points F

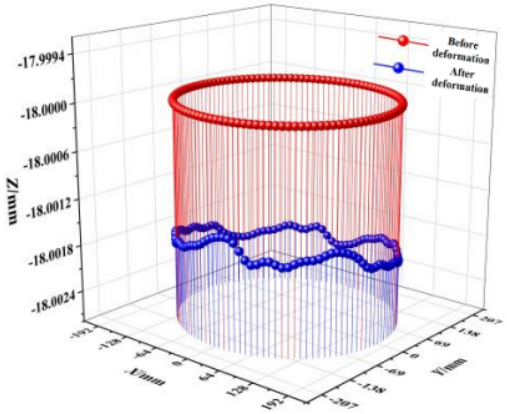

(g) Monitoring points G

Figure 27. Displacement deformation map of monitoring point($Q = 1.0Q_d$).

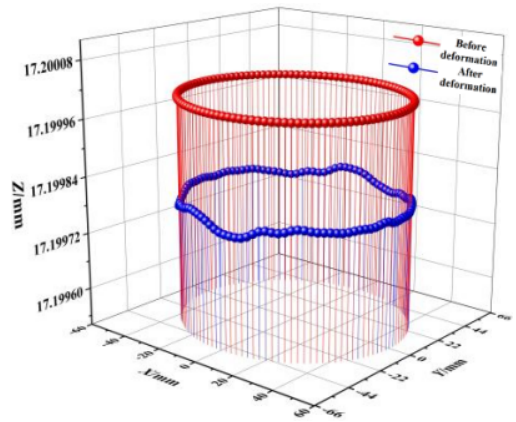

(a) Monitoring points A

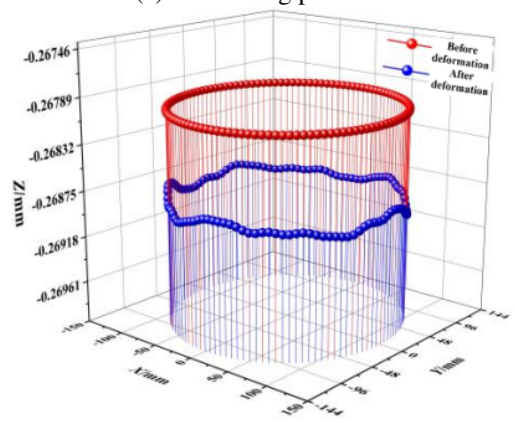

(b) Monitoring points B

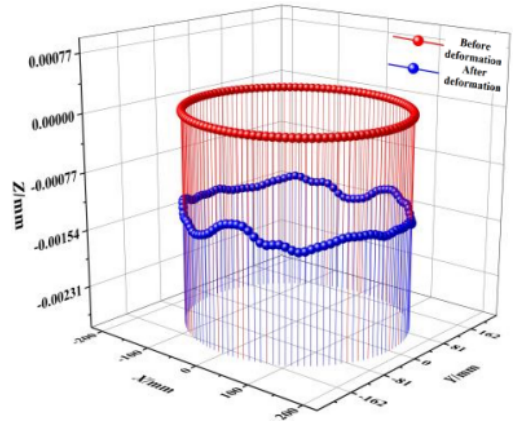

(c) Monitoring points C

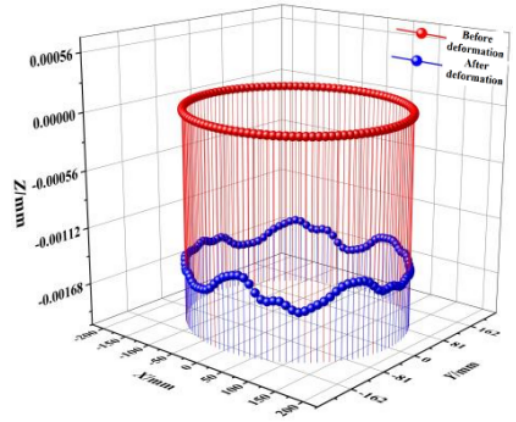

(d) Monitoring points D

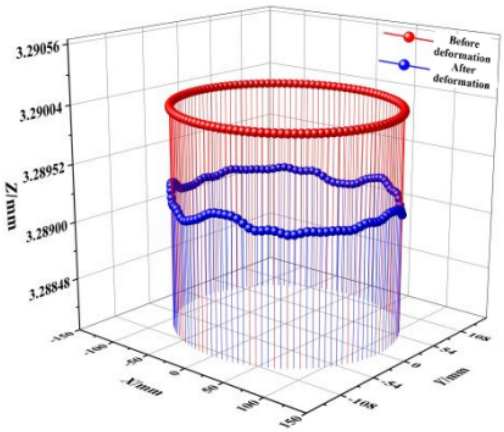

(e) Monitoring points E

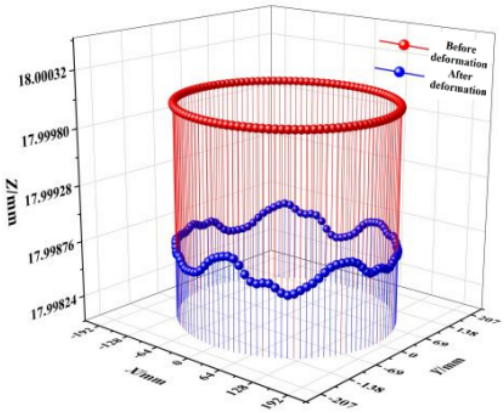

(f) Monitoring points F

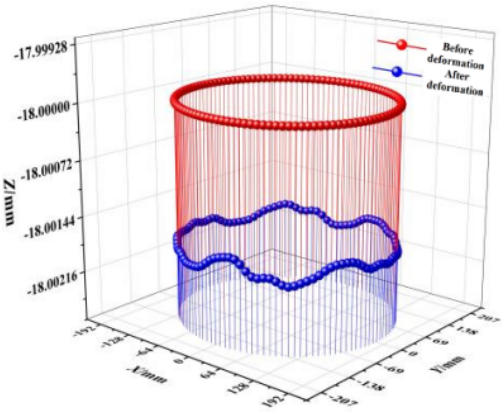

(g) Monitoring points G

Figure 28. Displacement deformation map of monitoring point($Q = 1.2Q_d$).